

# Electronic, Vibrational, and Structural Properties of a Spin-Crossover Catecholato–Iron System in the Solid State: Theoretical Study of the Electronic Nature of the Doublet and Sextet States

A. Jalila Simaan,<sup>[a]</sup> Marie-Laure Boillot,<sup>\*[a]</sup> Rosa Carrasco,<sup>[b]</sup> Joan Cano,<sup>[a]</sup> Jean-Jacques Girerd,<sup>[a]</sup> Tony A. Mattioli,<sup>[c]</sup> Jürgen Ensling,<sup>[d]</sup> Hartmut Spiering,<sup>[d]</sup> and Philipp Güttlich<sup>[d]</sup>

**Abstract:** As a functional model of the catechol dioxygenases, [(TPA)Fe(Cat)]BPh<sub>4</sub> (TPA = tris(2-pyridylmethyl)amine and Cat = catecholate dianion) exhibits the purple-blue coloration indicative of some charge transfer within the ground state. In contrast to a number of high-spin bioinspired systems, it was previously shown that, in the solid state, [(TPA)Fe(Cat)]BPh<sub>4</sub> undergoes a two-step  $S = 1/2 \rightleftharpoons S = 5/2$  spin-crossover. Therefore, the electronic and vibrational characteristics of this compound were investigated in the solid state by UV/Vis absorption and resonance Raman spectroscopies over the temperature range of the transition. This allowed the charge-transfer transitions of the low-spin (LS) form to be

identified. In addition, the vibrational progression observed in the NIR absorption of the LS form was assigned to a five-membered chelate ring mode. The X-ray crystal structure solved at two different temperatures, shows the presence of highly distorted pseudo-octahedral ferric complexes that occupy two nonequivalent crystalline sites. The variation of the molecular parameters as a function of temperature strongly suggests that the two-step transition proceeds by a successive transition of

the species in the two nonequivalent sites. The thermal dependence of the high-spin fraction of metal ions determined by Mössbauer experiments is consistent with the magnetic data, except for slight deviations in the high temperature range. The optimized geometries, the electronic transitions, vibrational frequencies, and thermodynamic functions were calculated with the B3LYP density functional method for the doublet and the sextet states. The finding of a ground state that possesses a significant mixture of Fe<sup>III</sup>-catecholate and Fe<sup>II</sup>-semiquinonate configurations is discussed with regard to the set of experimental and theoretical data.

**Keywords:** catechol dioxygenase • density functional calculations • iron • Raman spectroscopy • spin crossover

## Introduction

Fe<sup>III</sup>-catecholate systems have received considerable attention because their chemical properties mimic those of catechol dioxygenases<sup>[1]</sup> responsible for the oxidative cleavage of catecholate substrates. Studies of such functional models<sup>[2–5]</sup> have been directed toward the determination of their electronic and structural characteristics and their reactivity in order to clarify the role of the iron center in this enzyme. The studied compound<sup>[6]</sup> [(TPA)Fe(Cat)]BPh<sub>4</sub> (TPA = tris(2-pyridylmethyl)amine and Cat = catecholate dianion) exhibits the general features common to this class of compounds. For instance, the purple-blue coloration of solutions and solid samples at room temperature is attributed to the two strong absorption bands in the Vis/NIR range that are assigned to catecholate → Fe<sup>III</sup> charge-transfer tran-

[a] Dr. A. J. Simaan, Dr. M.-L. Boillot, Dr. J. Cano, Prof. J.-J. Girerd  
Laboratoire de Chimie Inorganique, UMR 8613, ICMO, Bât 420  
Université Paris-Sud, 91405 Orsay (France)  
Fax: (+33) 169-154-754  
E-mail: mboillot@icmo.u-psud.fr

[b] R. Carrasco  
Departament de Química Inorgànica, Universitat de València  
46100 Burjassot (València) (Spain)

[c] Dr. T. A. Mattioli  
SBE/DBJC and CNRS URA 2096, Bât 532  
CEA Saclay, 91191 Gif-sur-Yvette cedex (France)

[d] Dr. J. Ensling, Dr. H. Spiering, Prof. P. Güttlich  
Institut für Anorganische Chemie und Analytische Chemie, Johannes  
Gutenberg-Universität  
Staudingerweg 9, 55099 Mainz (Germany).

Supporting information for this article is available on the WWW  
under <http://www.chemurj.org/> or from the author.

sitions of the high-spin species. The energy of the lowest LMCT is obviously correlated with the extent of mixing between the Fe<sup>III</sup>-Cat and the Fe<sup>II</sup>-SQ forms (SQ = semiquinonate). This latter feature was considered to be important in the analysis of the *intradiol* cleavage activity in ferric catecholates compounds.<sup>[5b,7]</sup> Indeed, the model system [(TPA)-Fe(DBC)]BPh<sub>4</sub> (DBC = 3,5-di-*tert*-butylcatecholate dianion), isolated by Que and co-workers,<sup>[5c]</sup> exhibits the largest radical character in conjunction with the highest reactivity. This contribution was also mentioned by Funabiki and co-workers<sup>[7b]</sup> for chlorocatechol iron complexes. In this case, a smaller contribution of the Fe<sup>II</sup>-SQ form to the electronic ground state is associated with a lower reactivity, although the reaction with dioxygen proceeds catalytically. Different activation modes of the catechol ligand are presently debated and being investigated.<sup>[8]</sup>

Another interesting feature of [(TPA)Fe(Cat)]BPh<sub>4</sub> is the occurrence of a thermal spin-crossover in the solid state.<sup>[6]</sup> Indeed, the investigation of the magnetic properties has revealed a low-spin (LS) ⇌ high-spin (HS) crossover that arises in two steps. Spin-crossover compounds, especially iron(II) compounds, were extensively studied in the last two decades because, in the solid state, the reversible change of the spin multiplicity of the metal ion takes place through cooperative intermolecular interactions and leads to possible bistability and memory effects.<sup>[9]</sup> The thermal spin conversions, that are more or less quantitative as a consequence of the entropic excess in the high-spin state, give rise to different curves of the HS fraction ( $\gamma_{\text{HS}}$ ) versus temperature. For solid samples, the curves are continuous or discontinuous single step and discontinuous with a hysteresis effect.<sup>[10,11]</sup> This behavior is closely related to the solid-phase properties (cooperative interactions, phase transitions, structural defects, etc.).<sup>[11]</sup> In addition, two-step spin-crossover processes have been recognized for a few compounds, mainly mononuclear iron(II) compounds.<sup>[12-14]</sup>

Another potential interest of metal dioxolene systems is the possibility of valence tautomerism.<sup>[15,16]</sup> This requires the electronic levels of the transition metal ion and the redox active ligand, such as catecholate or semiquinonate (SQ<sup>-</sup>), to be close in energy and their electronic structures to be localized. The transformation, that was recognized for the Co<sup>II</sup>-SQ and Co<sup>III</sup>-Cat tautomers,<sup>[16]</sup> takes place through an intramolecular metal-ligand electron transfer combined with a spin-crossover of the metal ion.

Herein, we investigate the electronic, vibrational, and structural properties of [(TPA)Fe(Cat)]BPh<sub>4</sub> in the solid state to gain further insight into the nature of the electronic states and the changes associated with the thermally induced spin transition. The results of density functional molecular orbital calculations performed on the two spin isomers are also presented. They provide a set of data from which a new analysis of the experimental results<sup>[6]</sup> is proposed.

## Results and Discussion

**Temperature dependence of the optical properties:** Variable-temperature electronic absorption spectra were recorded for **1** dispersed in a KBr pellet. Prior to this, it was verified that no significant alteration resulted from the solid dispersion within the KBr matrix (see ref. [17] and Figure S1 in the Supporting Information). The absorption spectrum at 290 K (Figure 1) is similar to that recorded for a solution of

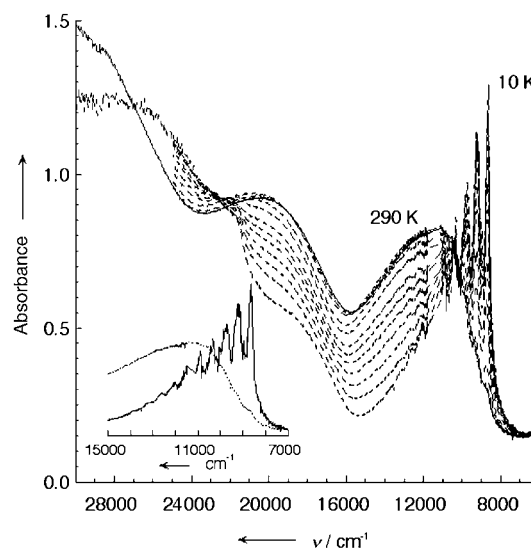


Figure 1. Temperature dependence of the UV/Vis-NIR spectrum of a KBr pellet of **1** recorded at 10, 50, 60, 70, 80, 90, 100, 120, 140, 200, 250, and 290 K. The optical density is plotted versus energy in cm<sup>-1</sup>. The inset shows the spectra recorded at 290 K (-----) and 10 K (—) expanded between 7000 and 15000 cm<sup>-1</sup>.

**1** in acetonitrile at room temperature.<sup>[6]</sup> Two broad bands are located at 11363 cm<sup>-1</sup> and 20408 cm<sup>-1</sup> (12531 cm<sup>-1</sup> and 19840 cm<sup>-1</sup>) for the solid sample (solution). It is notable that, at a lower energy, the NIR absorption is observed for the solid phase. The two bands responsible for the dark blue-violet color of these compounds are considered as typical for HS ferric-catecholate systems and are ascribed to spin-allowed catecholate-to-iron(III) charge-transfer transitions.<sup>[5b,18]</sup> Our DFT calculations (vide infra) suggest some revision of this classical analysis; however, these absorption bands will be named in the following as LMCT bands.

The temperature dependence of the solid-sample absorption spectra was monitored from 290 to 10 K. The evolution of the spectra as a function of temperature is also shown in Figure 1. The intensities of the visible and NIR LMCT bands markedly decrease with decreasing temperature. Parallel to this, a spectrum that is clearly detected in the NIR region from 275 K contains a new absorption band with a vibronic progression and gains in intensity when the temperature is lowered. The opposite intensity variation of these NIR absorption bands and the observation of pseudo-isosbestic points suggest the occurrence of a thermal equilibri-

um, namely the spin-crossover process characterized by the magnetic measurements.<sup>[6]</sup> To check this assertion, the relative area variation of the low-temperature NIR transition (components at 8678 cm<sup>-1</sup> and 9214 cm<sup>-1</sup>) was determined by deconvolution of the spectra and plotted as a function of the temperature (see Figure S2 in the Supporting Information). In spite of some inaccuracies (especially for area values at temperatures far from the transition temperature  $T_{1/2} = 92.5$  K), the tendency shown by this plot is consistent with the curves of  $\gamma_{\text{HS}}(T)$  deduced from the magnetic and Mössbauer data. The low-temperature spectrum is thus assigned to the LS species. We note that both the spin-crossover process of **1** and that of Schiff-base Fe<sup>III</sup> complexes<sup>[19]</sup> investigated in various matrices are characterized by a bathochromic shift (also supported by the computational result) of their LMCT in the low-temperature phase. The inset in Figure 1 shows the extension of the spectra recorded at 10 and 290 K. The intensity of the structured band found at low temperature compares well with that of the ligand-to-metal charge-transfer transition at high temperature. From these different features, the structured absorption band is assigned to a spin-allowed charge-transfer transition of the LS state of **1** (as confirmed by the RR and computational studies). One striking feature is the presence of at least eight or nine sharp transitions detected in the absorption band at 10 K. They are located at 8678, 9214, 9760, 10367, 10925, 11497, 12032, and 12590 cm<sup>-1</sup> and are almost regularly spaced at intervals of 520–560 cm<sup>-1</sup>. The intensities of the corresponding vibronic bands decrease from the low to the high energy side. This progression at low temperature indicates that there is, at least, one vibrational mode which is strongly coupled with the optical LMCT transition. From the space between successive components of the progression, it is deduced that this vibrational mode ( $\nu_0'$ ) of the excited state has a frequency of  $\approx 520\text{--}560$  cm<sup>-1</sup>.

**Temperature dependence of resonance Raman spectra:** Variable-temperature resonance Raman (RR) measurements have been performed to probe the nature of the vibrational mode coupled to the electronic transition. The RR spectra of **1** were recorded at two different excitation wavelengths, namely, 1064 and 752.5 nm, which are expected to preferentially enhance the Raman-active modes of the low-temperature and high-temperature forms, respectively.

*1064 nm excitation:* The RR spectrum of the LS form of **1** at 15 K (Figure 2) is dominated by a luminescent background exhibiting vibronic structure on which the narrower Raman bands are superimposed. These vibronic bands are much too broad ( $\approx 250$  cm<sup>-1</sup> FWHM) to correspond to vibrational Raman bands, and are similar in bandwidth and separation ( $\approx 500\text{--}550$  cm<sup>-1</sup>) to those observed in the low-temperature electronic absorption spectrum. The spectrum is uncorrected for detector response and the sharp cut-off seen at about 6000 cm<sup>-1</sup> ( $\approx 3000$  cm<sup>-1</sup> on Raman shift scale in Figure 2) is attributed to the drop in detector sensitivity. Although the relative intensities of the luminescence vibronic bands are

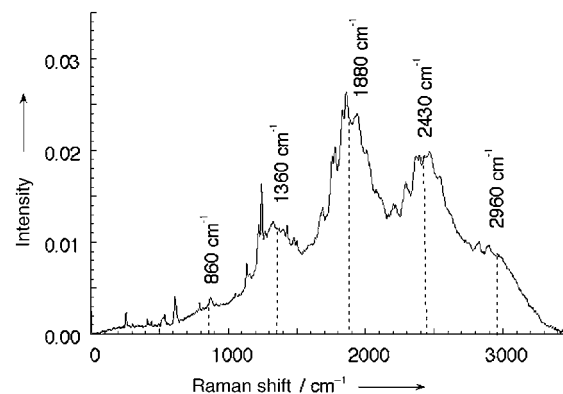


Figure 2. Resonance Raman spectrum of **1** recorded at 15 K with a 1064 nm excitation.

not strictly accurate, their observed frequencies and spectral separation will not be altered. From the superimposition of the electronic absorption spectrum and the luminescence spectrum (Figure 3), it is clear that there is a mirror symme-

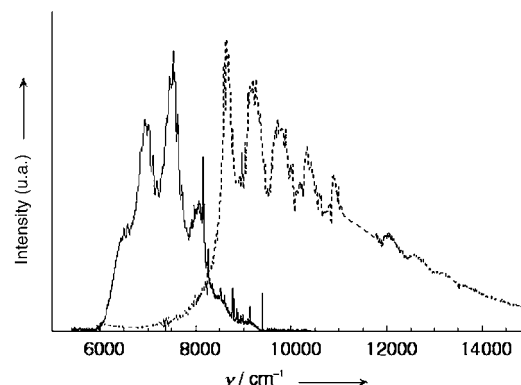


Figure 3. Comparison of the RR spectrum (1064 nm excitation) and the electronic absorption spectrum recorded at 15 and 10 K, respectively.

try which strongly suggests that the luminescence is a fluorescence spectrum (albeit very weak because the intensity is comparable to the RR band intensities). If we assume that the luminescence spectrum is caused by fluorescence, then we can estimate that the Stokes shift is about 620 cm<sup>-1</sup>. The observation of absorption and fluorescence spectra with strong vibronic progressions is consistent with an excited state undergoing a significant but not too large shift in its potential energy surface compared to the ground electronic state. Time-resolved measurements are required to provide conclusive evidence for the luminescence process exhibited by this ferric catecholate complex.<sup>[20]</sup>

Figure 4 shows a magnified view of the RR spectrum between 200 and 1500 cm<sup>-1</sup> for the low-spin form of **1** at 15 K. RR data for some other Fe<sup>III</sup>-catecholate complexes are reported,<sup>[5b,21–23]</sup> however, for all of these, the iron ion was in the HS state. To our knowledge, no RR data are reported for a LS Fe<sup>III</sup>-catecholate complex; we expect the frequen-

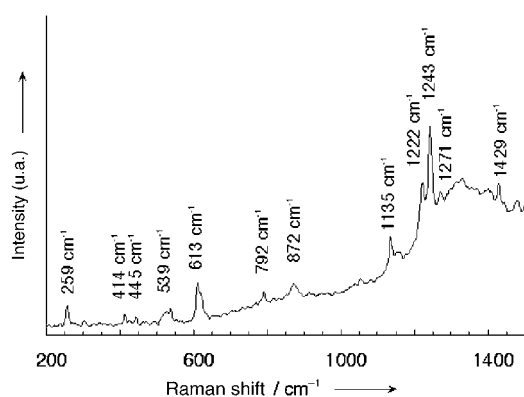


Figure 4. Magnified view of the RR spectrum between 200 and 1500  $\text{cm}^{-1}$  for the LS form of **1** (15 K, 1064 nm excitation).

cies to be different for LS and HS, although the change will not be large. The vibrational modes most enhanced in the RR spectrum correspond to those of the electronic ground state that mimic the distortion in the resonant excited electronic state.

The RR spectrum in Figure 4 exhibits a band at  $\nu = 539 \text{ cm}^{-1}$  with a broad shoulder at about  $520 \text{ cm}^{-1}$ . This band can be attributed to the five-membered chelate ring mode by comparison with HS complexes reported (also confirmed by the DFT calculations). Indeed, in  $\text{Fe}^{\text{III}}$ -catecholate systems, such a band has been observed between 509 and  $533 \text{ cm}^{-1}$ <sup>[21–23]</sup> and at  $528 \text{ cm}^{-1}$  for the  $[\text{Fe}(\text{oxalate})_3]^{3-}$  complex.<sup>[22]</sup> This mode represents a good candidate for the predominant mode responsible for the vibronic progression observed in the electronic absorption and fluorescence spectra. Thus the frequency of the optical transition-coupled vibrational mode in the fundamental low-spin state ( $\nu_0''$ ) seems to be  $539 \text{ cm}^{-1}$ . The most intense band in the low-frequency region is observed at  $613 \text{ cm}^{-1}$  with a shoulder at  $620 \text{ cm}^{-1}$ , which can be assigned to a deformation mode of the catecholate ring with Fe–O stretching character.<sup>[5b,21]</sup> The bands at 1140 and  $1431 \text{ cm}^{-1}$  are expected to arise from aromatic C–H deformation and C–C stretching modes, respectively.<sup>[5b,21]</sup> Based on calculations of  $\text{Fe}^{\text{III}}$ -catecholate complexes (this work, see Table 6 and ref. [23]), the  $792 \text{ cm}^{-1}$  band can be attributed to a catecholate mode. Vibrations with C–O character are expected at about  $1250 \text{ cm}^{-1}$ . Three bands are observed in this spectral region: 1223, 1245, and  $1270 \text{ cm}^{-1}$ . The 1223 and  $1245 \text{ cm}^{-1}$  bands could arise from the second overtone of the 613 or  $620 \text{ cm}^{-1}$  bands. However, no such overtone bands are significantly enhanced or observed for the  $520\text{--}539 \text{ cm}^{-1}$  bands. All the above observed frequencies are assignable to the low-spin form of the complex.

An increase in the temperature results in the broadening of the fluorescence background and loss of vibronic structure, as was observed in the electronic absorption spectrum. There are also significant changes observed in the Raman bands (see Figure S3 in the Supporting Information). In general, most of the RR bands lose intensity, with the exception

of the  $520\text{--}539$  and  $613\text{--}620 \text{ cm}^{-1}$  bands. This may be attributable to the change in RR enhancement conditions of the high-spin vibrational modes; because at high temperature, the absorption band dramatically changes in the region of  $1064 \text{ nm}$ , the wavelength of the Raman excitation laser. In addition, there are shifts observed in the Raman bands frequencies. The sharp band at  $539 \text{ cm}^{-1}$  is now replaced by a sharp band at  $521 \text{ cm}^{-1}$ . The band at  $613 \text{ cm}^{-1}$  along with the shoulder at  $620 \text{ cm}^{-1}$  appear to broaden into a more symmetric band centered at  $620 \text{ cm}^{-1}$ . In addition, the C–H deformation mode remains unshifted at  $1140 \text{ cm}^{-1}$ , whereas the C–C mode is shifted from  $1431$  to  $1445 \text{ cm}^{-1}$ . In the C–O stretching region, the three bands are now observed at 1213 (instead of 1223), 1245, and  $1298 \text{ cm}^{-1}$  (as compared to  $1270 \text{ cm}^{-1}$ ). The apparent lack of shift of the  $1245 \text{ cm}^{-1}$  band is consistent with non-shift of the  $620 \text{ cm}^{-1}$  band, assuming that the former is an overtone of the latter. The observed shifts can be interpreted as structural changes accompanying the conversion of the low-spin complex to the high-spin form as the temperature is raised. To better analyze the RR spectrum, we recorded variable-temperature RR spectra of the complex with  $752.5 \text{ nm}$  excitation, which is in resonance with the high-spin form absorption at high temperature.

**752.5 nm excitation:** Figure 5 shows the RR spectrum of **1** at 270 K with an excitation wavelength of  $752.5 \text{ nm}$ . As expected, the RR band frequencies observed here are similar to those obtained for the HS form with an excitation wavelength of  $1064 \text{ nm}$ .

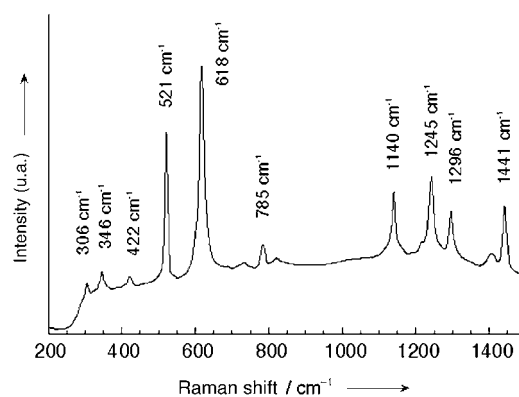


Figure 5. Magnified view of the RR spectrum between 200 and  $1500 \text{ cm}^{-1}$  for the HS form of **1** (270 K,  $752.5 \text{ nm}$  excitation).

RR spectra of **1** were recorded down to 10 K. Surprisingly, absolutely no changes in band positions are observed as the temperature is varied. This contrasts to the findings for the previous set of spectra (excited at  $1064 \text{ nm}$ ). Even at 15 K, the detected RR bands seem to be assignable to the HS form of **1** and no band indicative of a LS fraction was detected. Such an observation contradicts the magnetic measurements and suggests that, under these experimental conditions, some HS fraction is retained at low temperature. This HS fraction would be preferentially detected if one

considers the resonance conditions. The laser power at the sample being 50 mW, several hypotheses can be taken into account in order to explain this result. First, it can be assumed that under irradiation, the temperature of the sample is increased thus inducing conversion of a fraction of molecules into the HS state, even at 15 K. Second, it can also be assumed that the HS state is populated by an irradiation-pumped fundamental state. Indeed, the light-induced excited spin-state trapping effect,<sup>[24]</sup> which was demonstrated for a number of iron(II) spin-crossover complexes, was recently reported for a ferric spin-crossover complex.<sup>[25]</sup>

**X-ray diffraction:** Slow diffusion of diethyl ether into a CH<sub>3</sub>CN solution of **1** in the absence of molecular dioxygen afforded purple-blue and acicular crystals suitable for X-ray structural investigations. The crystal structure was solved at 220 and 110 K where the iron(III) ions are at least partly in the HS state ( $\gamma_{\text{HS}} \approx 0.92$  (220 K) and  $\approx 0.66$  (110 K)). The accuracy of both structures is limited by the quality of the crystals. Therefore, the present analysis is mainly restricted to the mean values of selected data and significant thermal evolutions. At both temperatures, the compound crystallizes in the orthorhombic space group *Pca2*(1) with *Z* = 8. The asymmetric unit contains two crystallographically independent sites (hereafter designated as A and B) that occur as general positions. Selected bond lengths and angles are listed in Table 1. Intermolecular distances shorter than the van der Waals distances and interatomic C–C distances for the  $\pi$ -stacking interactions are given in Tables S1 and S2 in the Supporting Information.

Table 1. Selection of bond lengths and angles for **1** in the crystallographic sites A and B.<sup>[a]</sup>

<i>T</i>	Site A		Site B	
	220 K	110 K	220 K	110 K
Fe–O1	1.90(1)	1.91(1)	1.90(1)	1.89(1)
Fe–O2	1.95(1)	1.92(1)	1.89(1)	1.91(1)
Fe–N2	2.10(1)	2.07(1)	2.12(1)	2.08(1)
Fe–N3	2.13(1)	2.07(1)	2.11(1)	2.07(1)
Fe–N4	2.14(1)	2.12(1)	2.09(1)	2.03(1)
Fe–N1	2.19(1)	2.19(1)	2.16(1)	2.08(1)
O1–C19	1.38(2)	1.39(2)	1.36(2)	1.34(2)
O2–C24	1.28(2)	1.33(2)	1.35(2)	1.33(2)
C19–C20	1.39(2)	1.40(2)	1.34(2)	1.36(2)
C20–C21	1.40(2)	1.39(2)	1.40(2)	1.43(2)
C21–C22	1.35(2)	1.35(2)	1.38(2)	1.39(2)
C22–C23	1.41(2)	1.40(2)	1.42(2)	1.38(2)
C23–C24	1.47(2)	1.41(2)	1.40(2)	1.42(2)
C24–C19	1.35(3)	1.39(2)	1.40(3)	1.41(3)
N1–Fe–N3	77.0(5)	77.3(5)	76.0(5)	79.3(5)
N1–Fe–N4	76.7(5)	78.1(4)	78.5(5)	81.2(5)
N1–Fe–O2	99.3(5)	98.3(4)	99.4(5)	96.9(5)
O1–Fe–N3	101.9(5)	100.8(5)	101.1(5)	98.3(5)
O1–Fe–N4	104.5(5)	103.9(5)	104.3(5)	101.2(5)
N3–Fe–N4	153.6(5)	155.3(5)	154.5(5)	160.4(5)

[a]  $\langle \text{Fe}_A\text{–L} \rangle = 2.07(2)$  Å (220 K) and  $2.05(2)$  Å (110 K),  $\langle \text{Fe}_B\text{–L} \rangle = 2.04(2)$  Å (220 K) and  $2.01(2)$  Å (110 K);  $\langle \text{C–O}_A \rangle = 1.33(2)$  Å (220 K) and  $1.36(2)$  Å (110 K);  $\langle \text{C–O}_B \rangle = 1.35(2)$  Å (220 K) and  $1.34(2)$  Å (110 K);  $\langle \text{C–C}_A \rangle = 1.40(2)$  Å (220 K) and  $1.39(2)$  Å (110 K);  $\langle \text{C–C}_B \rangle = 1.39(2)$  Å (220 K) and  $1.40(2)$  Å (110 K).

**Molecular structures:** At 220 K, the coordination sphere is almost the same for the cations occupying sites A and B. The metal center is coordinated to one amino (N1) and three imino (N2, N3, N4) nitrogen atoms of the tripodal ligand TPA and two oxygen (O1, O2) atoms of the catechololate (Figure 6). As indicated by the bond angles listed in

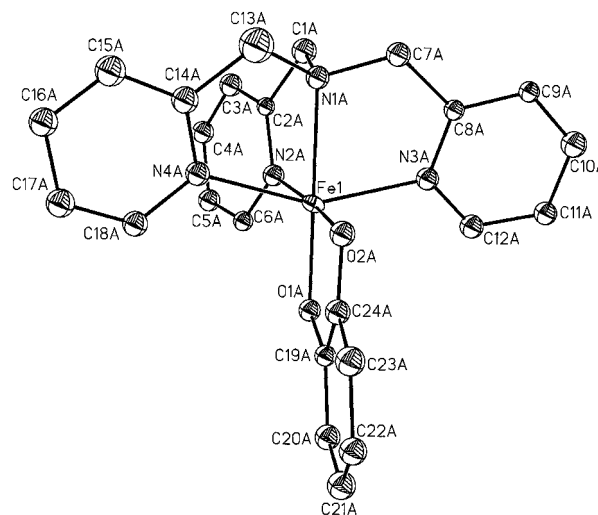


Figure 6. SHELXTL drawing of the Fe<sup>III</sup> ion in **1** at 220 K.

Table 1, both six-coordinate complexes are appreciably distorted from ideal octahedral geometry. The Fe–N<sub>amine</sub> bonds located *trans* to the Fe–O bonds are the longest at 2.19(1) (site A) and 2.16(1) Å (site B). The Fe–N<sub>pyridine</sub> bond lengths, with average values of 2.12(1) (A) and 2.11(1) Å (B), indicate some degree of  $\pi$ -backbonding with the pyridine rings. The average Fe–O bond lengths are 1.93(1) (A) and 1.90(1) (B) Å. This set of data is comparable to the corresponding set reported for HS Fe<sup>III</sup>–catechololate systems (Fe–N<sub>amine</sub> = 2.151–2.246, Fe–N<sub>pyridine</sub> = 2.109–2.227, Fe–O = 1.907–1.979 Å).<sup>[2–5,26]</sup> The studied compound displays a mean value of the C–O bond lengths of 1.33(2) (A) and 1.35(2) Å (B) (see Table 1), whereas the C–C bonds average at 1.40(2) (A) and 1.39(2) Å (B) and more specifically the C21–C22 bond is equal to 1.35(2) (A) and 1.38(2) Å (B). Although these values observed in **1** fall within the ranges corresponding to Fe<sup>III</sup>–catechololate systems,<sup>[5a,27,28]</sup> their low level of precision prevents us from unambiguously analyzing the catechololate or semiquinonate character of the dioxolene unit.

Some evolution becomes apparent in the X-ray data collected at 110 K. Significant changes of bond lengths and angles (Table 1) reflect the HS-to-LS conversion from 92 to 66% and the metal environment of the two cations are no more similar. For the cation A, the bond lengths and angles of the [FeN<sub>4</sub>O<sub>2</sub>] core vary between 220 and 110 K within the 3 e.s.d. limits and hence are not significant (see, for example, the data for the most compressible Fe<sub>A</sub>–N<sub>amine</sub> bond). From these characteristics, it is very likely that the cation in site A remains in the HS state at 110 K. In contrast, for site B, all the Fe<sub>B</sub>–N bond lengths decrease with decreasing tempera-

ture as a consequence of the depopulation of the antibonding  $e_g$  orbitals. The most significant variations are observed for the  $\text{Fe}_B\text{-N}_{\text{amine}}$  bond that is shortened from 2.16(1) (220 K) to 2.08(1) Å (110 K). The mean metal–ligand distance  $\text{Fe}_B\text{-L}$  of 2.01(1) Å (110 K) clearly lies between the values reported for iron(III) spin-crossover complexes ( $\text{Fe-L} = 2.058\text{--}2.074$  for HS species and 1.937–1.959 Å for LS species).<sup>[11,29]</sup> The values of the bond angles are found to be significantly closer to the values expected for ideal octahedral geometry. The  $\text{N}_3\text{-Fe}_B\text{-N}_4$  angle between the metal ion and the two opposite N donor atoms of TPA increases from 154.5(5) to 160.4(5)°. From these characteristics, it is inferred that site B is mostly occupied by LS species at 110 K and consequently only this site B is involved in the high-temperature transition. This analysis is also supported by the comparison between the value of the  $\text{Fe}_B\text{-N}_{\text{amine}}$  bond variation extrapolated for a complete conversion of the  $\text{Fe}_B$  ions ( $\sim 0.15$  Å for  $\Delta\gamma_{\text{HS}}(\text{B}) = 0.52$  and  $\Delta\gamma_{\text{HS}}(\text{A}) = 0$ ) and the corresponding one reported for iron(III) spin-crossover complexes ( $\approx 0.18$  Å).<sup>[11,29]</sup> The presence of crystallographically different iron(II) sites with slightly different spin-transition behavior, thus causing a step in the overall spin transition function  $\gamma_{\text{HS}}(T)$ , has been reported for other systems as well.<sup>[13,14]</sup> Other iron(II) complexes with crystallographically different lattice positions are known in which one type undergoes a thermal spin transition while the other one remains in the HS state at all temperatures. Of course, these systems do not show a step in the  $\gamma_{\text{HS}}(T)$  curve, instead

$\gamma_{\text{HS}}(T)$  merges into a plateau at low temperature at  $\gamma_{\text{HS}}$  values depending on the concentration ratio of the different lattice sites.<sup>[30]</sup> Note that the ordering of the spin states at very low temperatures can not be extrapolated from the present results as this process may be coupled to an order-disorder phase transition giving rise to a new distribution of the iron sites.

**Intermolecular interactions:** In Figure 7, the packing of **1** in the *ac* plane consists of successive layers along the *c* axis that contain one sort of cation or anion. At 220 K, the closer intermetallic distance is found for  $\text{Fe}_A\text{Fe}_B = 9.099(3)$  Å along the *c* axis (9.094(3) at 110 K). For the cations occupying the same site (A or B), these distances are equal to 9.449(2) Å at 220 K (9.400(2) Å at 110 K). Rather strong  $\pi$ -stacking interactions ( $\text{C-C}$  distances  $< 3.50$  Å) and a number of intermolecular  $\text{C}\cdots\text{C}$  contacts are identified (see Tables S1 and S2 in the Supporting Information). These structural parameters that strongly favor the cooperative interactions and the abrupt transition curves,<sup>[31]</sup> are strengthened at low temperature. This feature is in agreement with some reinforcement of the cooperativity at 110 K.

**Mössbauer measurements:** The Mössbauer spectra of **1**, recorded between 293 and 1.9 K, are displayed in Figure 8. The least-squares-fitted parameters are collected in Table 2. At temperatures between 293 and 190 K, the spectra consist of a quadrupole doublet with a mean value of the isomer shift  $\delta \approx 0.43$   $\text{mm s}^{-1}$  and the quadrupole splitting  $\Delta E_Q = 1.30$   $\text{mm s}^{-1}$ . These values compare to those given for compounds of biological interest.<sup>[32]</sup> However, we note that such a value of  $\Delta E_Q$  is reported either for hexacoordinate  $\text{Fe}^{\text{III}}\text{-Cat}$  complexes with a high electric field gradient that is attributed to a distorted coordination core<sup>[33]</sup> or for HS  $\text{Fe}^{\text{III}}\text{-SQ}$  compounds.<sup>[28a,34]</sup> The doublet shows the typical features of slow paramagnetic relaxation of  $\text{Fe}^{\text{III}}$  in the high-spin state which results in different broadening of the lines with decreasing temperature. Below 50 K, only the doublet characteristic for LS  $\text{Fe}^{\text{III}}$ <sup>[32]</sup> ( $\delta = 0.255 \pm 0.017$   $\text{mm s}^{-1}$  and  $\Delta E_Q = 1.881 \pm 0.023$   $\text{mm s}^{-1}$ ) is detected with a small asymmetry in the intensities of the two lines, which is most probably caused by textural effects of the acicular crystals of the compound. A fit with two doublets gives

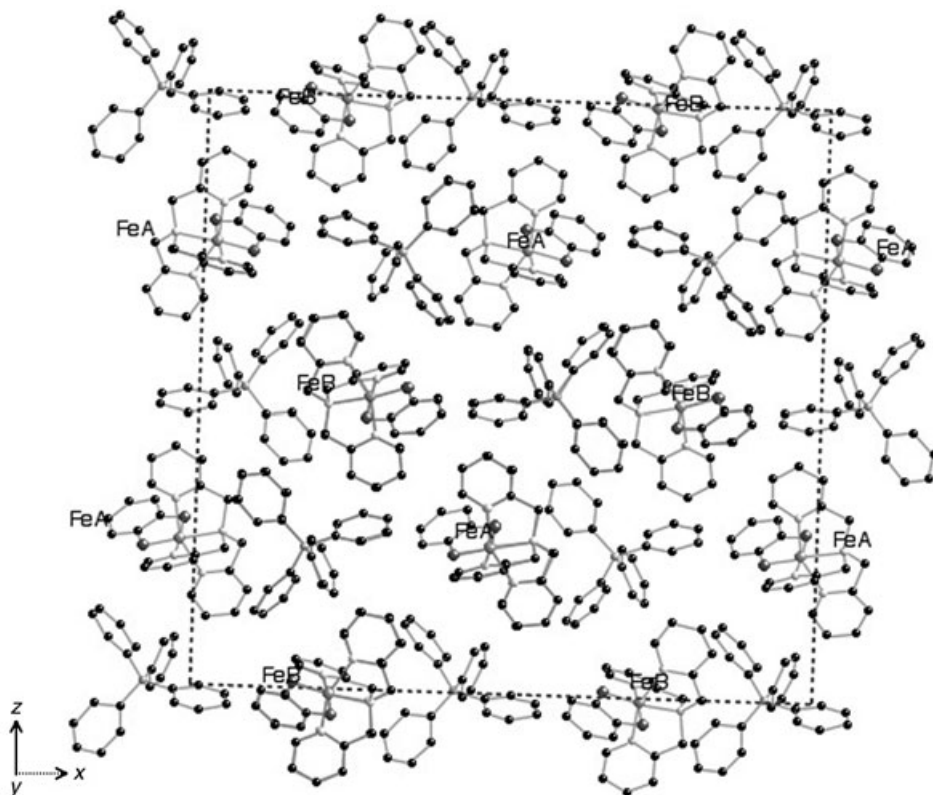


Figure 7. Packing diagram of **1** at 220 K in the *ac* plane. Hydrogen atoms are omitted for clarity.

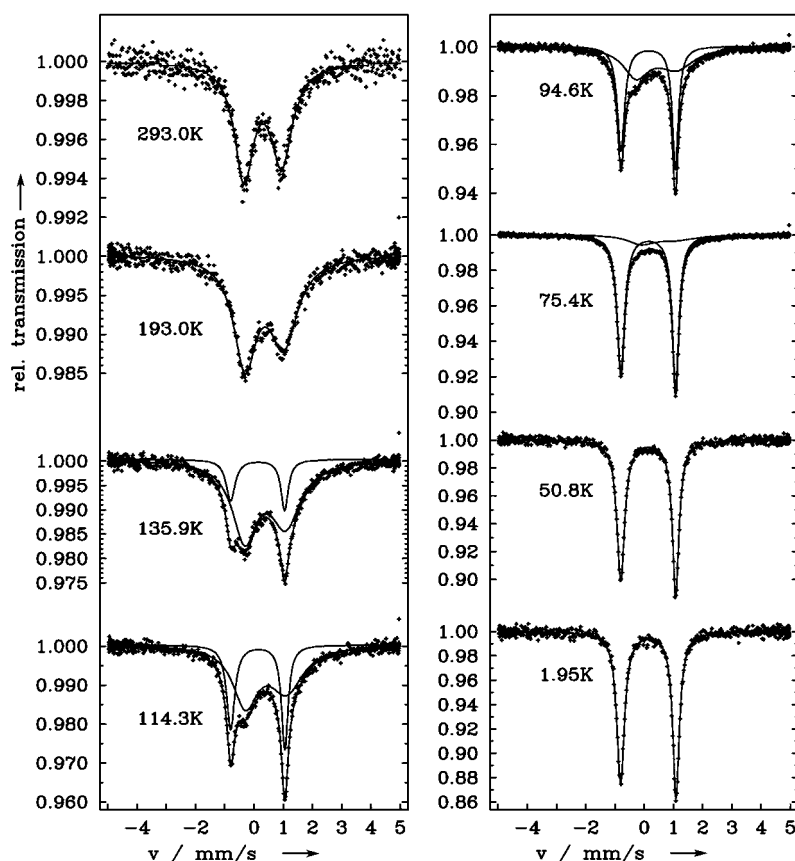


Figure 8.  $^{57}\text{Fe}$  Mössbauer spectra recorded at 293, 193, 135.9, 114.3, 94.6, 75.4, 50.8, and 1.95 K.

Table 2. Selected  $^{57}\text{Fe}$  Mössbauer fitted parameters of **1**. Isomer shifts are relative to Fe metal. The HS fraction is based on the evaluation of the areas  $A_{\text{HS}}$  and  $A_{\text{LS}}$  the HS and LS resonance lines, assuming equal Lamb–Mössbauer factors for the two spin states.

$T$ [K]	$\delta^{\text{S}}(\text{LS})$ [ $\text{mm s}^{-1}$ ]	$\Delta E_{\text{O}}(\text{LS})$ [ $\text{mm s}^{-1}$ ]	$\delta^{\text{S}}(\text{HS})$ [ $\text{mm s}^{-1}$ ]	$\Delta E_{\text{O}}(\text{HS})$ [ $\text{mm s}^{-1}$ ]	HS fraction
293	–	–	0.412(5)	1.286(2)	1
193.3	–	–	0.462(13)	1.315(22)	1
135.9	0.235(10)	1.842(21)	0.495(18)	1.398(25)	0.836(25)
114.3	0.239(43)	1.847(9)	0.523(27)	1.407(33)	0.679(37)
94.6	0.249(19)	1.859(4)	0.526(31)	1.379(40)	0.498(27)
75.4	0.2491(8)	1.870(1)	0.584(54)	1.381(81)	0.175(15)
50.8	0.249(3)	1.874(2)	–	–	0
4.2	0.251(2)	1.881(2)	–	–	0

slightly different isomer shifts and quadrupole splittings with almost overlapping error limits ( $\delta_1 = 0.258 \pm 0.014 \text{ mm s}^{-1}$ ,  $\Delta E_{\text{O}1} = 1.870 \pm 0.030 \text{ mm s}^{-1}$ , and  $\delta_2 = 0.242 \pm 0.010 \text{ mm s}^{-1}$ ,  $\Delta E_{\text{O}2} = 1.820 \pm 0.025 \text{ mm s}^{-1}$ ) at 4.2 K. Between 190 and 50 K, a superimposition of the resonance lines for HS and LS  $\text{Fe}^{\text{III}}$  is observed. The fit in the transition temperature range takes into account the magnetic relaxation of the HS  $\text{Fe}^{\text{III}}$ , and assumes a static behavior of  $\text{Fe}^{\text{III}}$  in the LS state. In Figure 9, the area fraction of the HS doublet is plotted versus temperature, taking equal recoil-free fractions for HS and LS species. These data agree with the results of the magnetic measurements, except for slight deviations in the high-temperature range.

bond lengths with respect to the experimental geometries, an effect that is more pronounced for the HS state. Indeed DFT calculations were performed by considering an isolated molecule, although molecules in a solid phase undergo a “chemical pressure” due to the packing forces. This effect is critical in spin-crossover systems because of the energy proximity of the HS and LS levels. Moreover, the difference between the structural parameters of the LS and HS states is associated with the entropy variation that controls the extent of the LS-to-HS conversion. Therefore, the experimental molecular volume at any temperature is always smaller than that of the pure HS state, a fortiori for an isolated molecule.

The fits of the low-temperature Mössbauer data do not show strong evidence for two different crystallographic sites of  $\text{Fe}^{\text{III}}$ ; however, the existence of two sites can not be excluded.

### DFT calculations

**Molecular geometry:** In Table S3 in the Supporting Information, a selection of structural data for **1** and  $[(\text{TPA})\text{Fe}(\text{Cl}_4\text{Cat})]\text{PF}_6$  (**2**)<sup>[35,36]</sup> spin-crossover complexes shows the corresponding coordination spheres in the experimental and optimized geometries (for HS and LS states). Despite some structural differences, good agreement is found. As expected, the metal–ligand bond lengths are shortened in the LS state and the symmetry of the metal environment is broken as a consequence of the chelation of the TPA ligand (L'). This asymmetry observed in the coordination core is extended over the catechol ligand. From the X-ray crystal structures reported so far, this feature appears to be common to this class of compounds. The agreement between experimental and theoretical (optimized geometry) results is better for **2** as a consequence of the completeness of the spin transition and the accuracy of the structural data of **2**.<sup>[36]</sup> Nevertheless, in all cases, the optimized geometries lead to the longest metal–ligand

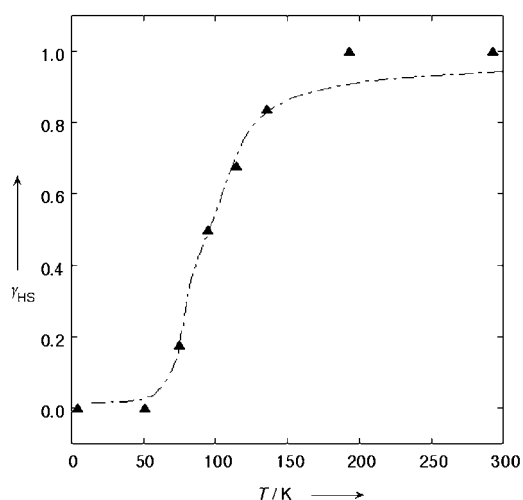


Figure 9. Temperature dependence of the HS fraction  $\gamma_{\text{HS}}$  ( $\blacktriangle$ ) for **1** deduced from the fractional area  $a_{\text{HS}}$  of the Mössbauer components. The curve of  $\gamma_{\text{HS}}(T)$  (---) was calculated from the magnetic data by assuming  $\chi_{\text{M}}T_{\text{LS}} \sim 0.375$  and  $\chi_{\text{M}}T_{\text{HS}} = 4.375 \text{ cm}^3 \text{ mol}^{-1} \text{ K}$ .

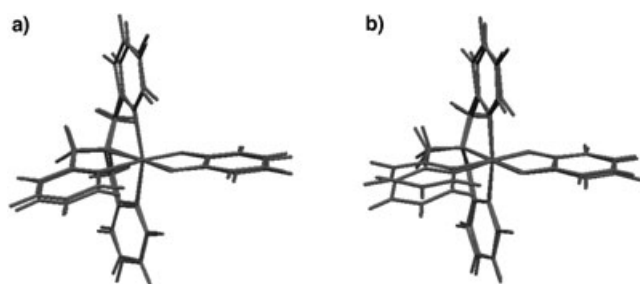


Figure 10. Superimposition of the optimized and experimental geometries for: a) the HS spin state and b) the LS spin state. The experimental geometries are based on those determined from the crystal structure of **1**.

Figure 10 shows the superimposition of the optimized and experimental geometries for the molecular cation  $[(\text{TPA})\text{Fe}(\text{Cat})]^+$ . The agreement between both geometries clearly extends over the complete molecular skeleton, including the relative disposition of the aromatic groups in the TPA ligand. A negligible discrepancy, which consists of a pyridine group in TPA slightly deflected from the experimental position, is found in the LS state. This is attributed to the shorter metal–ligand bond lengths in the LS state and the reduced molecular flexibility in the solid phase.

As previously mentioned, the bond lengths in the dioxolene ligand (noted L) are closely related to its oxidation state. Delocalized  $\pi$  bonds are characterized for the aromatic ring of a catecholato dianion and a quinoid-type pattern with localized  $\pi$  bonds is found in semiquinonato radicals.<sup>[5c,28d,37]</sup> Another criterion is based on the specific values of the C4–C5 bond length, which depends on the oxidation state of the catechol ligand (1.369–1.400 Å, for  $\text{L} = \text{Cat}^{2-}$  and 1.383–1.446 Å for  $\text{L} = \text{SQ}^{\cdot-}$ ). In contrast to the X-ray crystallographic data obtained for **1** that provides an ambiguous result (see above), the analysis of the optimized structures reveals a clearer situation. In Table 3, we compare the

Table 3. Bond lengths found in the catechol ring. The C atoms linked to the oxygen atoms are labeled 1 and 2. Therefore, in the structural data available for  $[(\text{TPA})\text{Fe}(\text{Cat})]\text{BPh}_4$  (**1**), C21 and C22 should be replaced by C4 and C5 atoms.  $[\text{Fe}(\text{L}-\text{N}_4\text{Me}_2)(\text{Cat})]^+$  (**3**),  $[\text{Fe}(\text{L}-\text{N}_4\text{Me}_2)(\text{DBC})]^+$  (**4**),  $[\text{Fe}(\text{L}-\text{N}_4\text{Me}_2)(\text{DBSQ})]^{2+}$  (**5**), and  $[(\text{TPA})\text{Fe}(\text{DBC})]\text{BPh}_4 \cdot \text{CH}_3\text{CN}$  (**6**) complexes where  $\text{L}-\text{N}_4\text{Me}_2 = N,N'$ -dimethyl-2,11-diaza[3,3]-(2,6)pyridinophane and  $\text{DBSQ} = 3,5$ -di-*tert*-butylsemiquinone.

	<b>1</b> optimized LS	<b>1</b> optimized HS	<b>3</b>	<b>4</b>	<b>5</b>	<b>6</b>
C1–C2	1.440	1.440	1.415	1.411	1.450	1.418
C2–C3	1.415	1.409	1.385	1.380	1.403	1.382
C1–C6	1.416	1.413	1.394	1.409	1.425	1.405
C3–C4	1.395	1.400	1.427	1.393	1.360	1.390
C5–C6	1.395	1.398	1.369	1.396	1.370	1.403
C4–C5	1.425	1.419	1.369	1.399	1.438	1.395

results obtained from optimized geometries in the LS and HS states with those reported for compounds very similar to **1**.<sup>[28d]</sup> For these complexes,  $[\text{Fe}(\text{L}-\text{N}_4\text{Me}_2)(\text{Cat})]^+$  (**3**),  $[\text{Fe}(\text{L}-\text{N}_4\text{Me}_2)(\text{DBC})]^+$  (**4**), and  $[\text{Fe}(\text{L}-\text{N}_4\text{Me}_2)(\text{DBSQ})]^{2+}$  (**5**),  $[(\text{TPA})\text{Fe}(\text{DBC})]\text{BPh}_4 \cdot \text{CH}_3\text{CN}$  (**6**) (where  $\text{L}-\text{N}_4\text{Me}_2 = N,N'$ -dimethyl-2,11-diaza[3,3]-(2,6)pyridinophane and  $\text{DBSQ} = 3,5$ -di-*tert*-butylsemiquinone), the dioxolene ligand was identified as a catecholate (**3**, **4**, **6**) and a semiquinonate (**5**) (see Table 3). These data show that, for the optimized geometries of  $[(\text{TPA})\text{Fe}(\text{Cat})]^+$  in the HS and LS states, the observed alternating bond character is less pronounced than for **5**, and the C4–C5 bond length values are intermediate between those expected for the catechol and semiquinone forms. Thus, this structural analysis suggests that, in the  $S = 1/2$  and  $5/2$  states, **1** is present as an intermediate form between  $\text{Fe}^{\text{III}}\text{Cat}$  and  $\text{Fe}^{\text{II}}\text{SQ}$  configurations. A similar analysis is possible on the basis of the C1–C2 bond length.

**Electronic configuration:** The description of the electronic configuration of a coordination compound is quite straightforward when the organic ligands (spectator ligands) introduce small modifications in the properties of the metal ion. In contrast, some ligands (such as orthoquinone and its reduced forms)<sup>[15]</sup> have a strong influence on the electronic structure of the complex. In such cases, the frontier molecular orbitals, both of the ligand and the metal ion, are usually energetically close, that is, ligand and metal ion have comparable redox potentials. This situation may consist of two well-balanced orbital energies that allow the intersite exchange of one electron. The relative stability of the two electronic configurations can be finely tuned by a slight alteration of the metal environment or of the electron-acceptor character of the ligand. Thus the electronic density of the singly occupied molecular orbital (SOMO) may be centered either on the metal fragment (leading, for example, to the LS  $\text{Fe}^{\text{II}}\text{SQ}$  configuration) or on the ligand skeleton (LS  $\text{Fe}^{\text{III}}\text{Cat}$  configuration). Thus, these systems can display bi-stability (valence tautomeric interconversion).

Figure 11 shows the energy level diagram of the frontier molecular orbitals of the optimized  $[(\text{TPA})\text{Fe}(\text{Cat})]^+$  complex in the LS state. Between the occupied  $t_{2g}$  and the unoccupied  $e_g$  orbitals, several Cat and TPA antibonding  $\pi$ -orbi-



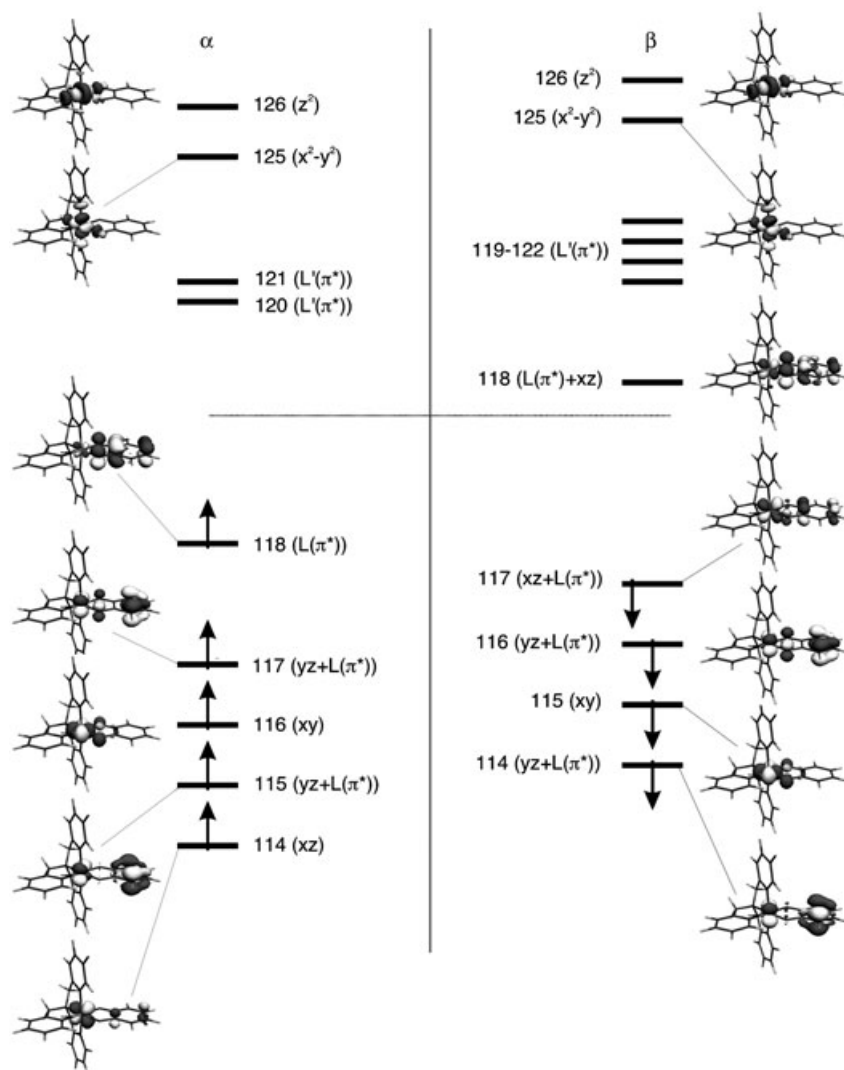


Figure 11. Semiquantitative energy level diagram of the frontier molecular orbitals of the LS state for the optimized  $[\text{Fe}(\text{TPA})(\text{Cat})]^+$  complex. The vertical and horizontal dashed lines separate the  $\alpha$  and  $\beta$  and the occupied and unoccupied MOs, respectively. The labels L and L' are used to denote MOs whose electronic densities are placed mainly on the Cat and TPA ligands, respectively.

tals ( $\pi^*(\text{L})$  and  $\pi^*(\text{L}')$ , respectively, are observed. The more stable orbital belongs to the catechol ligand. Note that the *alpha* HOMO (118 $\alpha$ ) is not a d orbital, but an orbital localized on the catechol ligand.

However, some catechol and d-metal orbitals are so close in energy that they intermix, that is, the electronic density is delocalized in each orbital on both the metal fragment and the catechol group (117 $\alpha$  and 115 $\alpha$ ). A similar situation is found in the *beta*-spin orbitals, where the HOMO (117 $\beta$ ) and LUMO (118 $\beta$ ) are totally delocalized. In this way, the system does not exhibit valence tautomerism but, rather, an intermediate situation between the  $\text{Fe}^{\text{III}}\text{Cat}$  and  $\text{Fe}^{\text{II}}\text{SQ}$  configurations, that is, a strong covalency is displayed.

A qualitative scheme for the electronic configuration in the HS state can be generated from the diagram shown in Figure 11. Two electrons should be added to the  $d_{x^2-y^2}$

(125 $\alpha$ ) and  $d_{z^2}$  (126 $\alpha$ ) *alpha* orbitals, whereas two others are removed from the  $d_{xy}$  (115 $\beta$ ) and  $d_{yz}$  (114 $\beta$ +116 $\beta$ ) *beta* orbitals. The only *beta* d orbital (117 $\beta$ ) that remains occupied is strongly delocalized on the catechol ligand. Thus, as previously found for the LS state, the HS state can be described as a mixture of the  $\text{Fe}^{\text{III}}\text{Cat}$  and  $\text{Fe}^{\text{II}}\text{SQ}$  configurations.

The NBO analysis of the atomic spin density is shown in Table 4. A priori, the metal spin density ( $\rho(\text{Fe})$ ) in a complex is partially delocalized on the ligands, decreasing its value with regard to the free metal ion. However, the NBO analysis shows that, in the doublet and sextet states, the atomic spin density on the iron ion is much smaller than the value expected for a free  $\text{Fe}^{\text{III}}$  ion. Thus, the pure  $\text{Fe}^{\text{III}}\text{Cat}$  configuration can be ruled out. In addition, we note that, in spite of the spin delocalization on the TPA ligand, in both HS and LS states,  $\rho(\text{Fe})$  is too high to be assigned to a  $\text{Fe}^{\text{II}}$  form and too low to be assigned to a  $\text{Fe}^{\text{III}}$  form. Thus, these results provide evidence for a mixture of a  $\text{Fe}^{\text{III}}\text{Cat}$  and a  $\text{Fe}^{\text{II}}\text{SQ}$  configurations for both spin states. It appears that the spin density on the catechol ligand ( $\rho(\text{L})$ ) of **1**

Table 4. Atomic spin densities for the HS and LS states of **1** in the experimental (single point) and optimized geometries. Cat refers to the total spin density for the catechol ligand.

	Single point		Optimized geometry	
	HS	LS	HS	LS
Fe	4.021	0.388	3.989	0.345
O1	0.275	0.218	0.276	0.203
O2	0.290	0.196	0.310	0.219
Cat	0.748	0.661	0.799	0.699

has an intermediate value between the values expected for a diamagnetic and a radical species. However, the radical character of L is more pronounced than expected, especially in the HS state. In all cases, the spin density on the catechol ligand (L) is mainly localized on the oxygen atoms ( $\approx 63\%$

73%) and the rest is nearly equally distributed throughout the carbon atoms. DFT calculations on the experimental geometry lead to the same conclusion (Table 3).

Recently, Rodriguez et al. have studied the complex  $[\text{Cr}(\text{tren})(3,6\text{-DTBSQ})]^{2+}$  (DTBSQ = 3,6-di-*tert*-butylortho-semiquinone) that has been unambiguously identified as  $\text{Cr}^{\text{III}}\text{SQ}$ .<sup>[38]</sup> A NBO analysis from the DFT calculations clearly shows the presence of the semiquinone radical. The authors have found large spin densities on the organic skeleton of the 3,6-DTBSQ ligand, whose distribution is similar to the one found in the free semiquinone. In the same way, we have performed DFT calculations on the free semiquinone from the experimental geometries. This leads to a distribution of spin density which is mainly centered on the O, C $\beta$ , and C $\gamma$  atoms with small negative values observed on the C $\alpha$  atoms, these features being typical of a free semiquinone radical. Although slight similarities are found between the calculated spin distribution in the complex and in the free semiquinone (see Table 5), it can neither be assigned to a

Table 5. Mean values of atomic spin densities in the L organic skeleton for the HS and LS states of **1** and free semiquinone. The geometries used in the DFT calculations have been taken from the experimental crystal structure of **1**.  $\alpha$ ,  $\beta$ ,  $\gamma$  designate the C1 or two, C6 or three, C5 or four carbon atoms, respectively.

	LS		HS	
	Complex <b>1</b>	Free semiquinone	Complex <b>1</b>	Free semiquinone
O	0.207	0.363	0.282	0.372
C $\alpha$	0.070	-0.023	0.036	-0.031
C $\beta$	-0.010	0.104	0.016	0.120
C $\gamma$	0.068	0.068	0.042	0.107

semiquinone radical in a  $\text{Fe}^{\text{II}}\text{SQ}$  form nor to a spin delocalization from the metal ion to the catechol ligand in the  $\text{Fe}^{\text{III}}\text{-Cat}$  form. It is closer to an intermediate situation. Moreover, we have observed a weak spin delocalization on the N-donor atoms of the TPA ligand. The spin delocalization and spin polarization are negligible on the other atoms of the aromatic rings. Finally, it is concluded that complex **1** in the HS and LS states should be described as a mixture of  $\text{Fe}^{\text{III}}\text{-Cat}$  and  $\text{Fe}^{\text{II}}\text{SQ}$  configurations or, in the framework of the molecular orbital theory, as a strongly covalent system. Although the determination of their respective weights appears to be a difficult task, our results based on the analysis of the molecular orbitals strongly suggest quasi-equivalent contributions of the  $\text{Fe}^{\text{II}}\text{SQ}$  and  $\text{Fe}^{\text{III}}\text{Cat}$  forms.

Some results reported in the literature indicate that some iron(II) complexes containing TPA or closely analogous ligands also exhibit spin-crossover processes.<sup>[39-41]</sup> For example,  $(\text{TPA})\text{Fe}(\text{NCS})_2$  presents an abrupt thermally-induced spin crossover centered at 170 K.<sup>[9e,40]</sup>

**Magnetic exchange interaction:** In a pure  $\text{Fe}^{\text{II}}\text{SQ}$  configuration, an antiferromagnetic interaction between the HS metal ion and the semiquinone radical can be expected as a consequence of the strong overlapping between the  $d_{xz}$  metal and

$\pi^*$  catecholate orbitals. Thus, the  $S = 3/2$  state should be more stable than the  $S = 5/2$  (HS) state. However, there is no experimental evidence for a  $S = 3/2$  state. From these results, it is inferred that the HS state corresponds either to a  $\text{Fe}^{\text{III}}\text{Cat}$  configuration or to a HS  $\text{Fe}^{\text{II}}$  ion that is ferromagnetically coupled with the semiquinone radical. The previous analysis of the electronic structure clearly rejects the first option. In addition, some of us have shown in a previous paper that a strong delocalization or an electron transfer may stabilize a particular spin state.<sup>[42]</sup> Thus, in the  $\text{Fe}^{\text{II}}\text{SQ}$  configuration (the  $\text{Fe}^{\text{II}}$  ion being in the HS state) a delocalization of the *beta* electronic density from the  $d_{xz}$  metal orbital to the  $\pi^*$  semiquinone orbital occurs. This delocalization, in the framework of the localized orbitals, can be seen as an interaction between the two configurations ( $\text{Fe}^{\text{II}}\text{SQ}$  and  $\text{Fe}^{\text{III}}\text{-Cat}$ ). We note that this delocalization is not possible in the  $S = 3/2$  state because the  $\pi^*$  semiquinone *beta* orbital is occupied. Other delocalizations are possible; however, they lead to excited states for the metal ion. In conclusion, only the  $S = 5/2$  state of the  $\text{Fe}^{\text{II}}\text{SQ}$  form will be stabilized.

Other features that also support this conclusion are the following. The  $S = 3/2$  state, which was calculated from the optimized geometry found for the  $S = 5/2$  state, should be present in a fully localized  $\text{Fe}^{\text{II}}\text{SQ}$  form. Thus, the calculated spin density on the metallic center ( $3.73 e^-$ ,  $S = 3/2$  state) is found to be slightly lower than the spin density on a HS  $\text{Fe}^{\text{II}}$  free ion as a consequence of the weak spin delocalization from the  $e_g$  orbitals to the TPA and  $\text{SQ}^-$  orbitals. The spin density on the  $\text{SQ}^-$  ligand is close to that of a radical. Moreover, the calculated  $S^2$  value for the quartet state (4.75) corresponds to that expected for a broken-symmetry function, that is, to a HS  $\text{Fe}^{\text{II}}$  ion antiferromagnetically coupled to a semiquinone radical. In order to establish the electronic nature of the sextet and doublet states, we can compare the spin densities on the semiquinone ligand for the case of the sextet, quartet, and doublet states. To avoid the effect of spin delocalization from the  $e_g$  orbitals, we have only considered the spin density values on the C1, C2, C4, and C5 atoms. These atomic spin density values are twice as large as those found in the sextet and doublet states. In agreement with our hypothesis, the magnetic exchange interaction between the HS  $\text{Fe}^{\text{II}}$  ion and semiquinone radical in **1** is ferromagnetic and the evaluated exchange coupling ( $H = -JS1S2$ ) is equal to  $+3510 \text{ cm}^{-1}$ . In conclusion, the doublet and sextet states correspond to an almost equal mixture of the  $\text{Fe}^{\text{II}}\text{SQ}$  and  $\text{Fe}^{\text{III}}\text{Cat}$  configurations.

**Thermal spin-crossover process:** For the optimized geometry, the doublet–sextet splitting, which is calculated from the minimum point of the potential energy curves ( $\Delta E_{\text{el}}^{\text{HL}} = E_{\text{el}}^{\text{HS}} - E_{\text{el}}^{\text{LS}}$ ), is found to have a positive value ( $178 \text{ cm}^{-1}$ ). The description of the total electronic energy at zero temperature ( $E_{\text{el}}(v = 0)$ ), implies an additional zero-point energy correction that takes account of the corresponding vibrational term ( $E_{\text{el}} + E_{\text{vib}}(T = 0)$ ). At this stage, the doublet–sextet splitting  $\Delta E_{\text{el}}^{\text{HL}}(v = 0)$  is found to be negative, which indicates a more stabilized sextet state. This feature

should preclude any spin-crossover process for **1** because the free enthalpy calculated at any temperature from the  $\Delta E_{\text{el}}^{\text{HL}}(0)$ ,  $\Delta E_{\text{vib}}^{\text{HL}}(T)$ , and  $\Delta S^{\text{HL}}(T)$  terms is always negative and, consequently, only the HS state is occupied. However, it is well established that the total energies  $E_{\text{el}}(0)$  provided by DFT calculations markedly deviate from the experimental energy values.<sup>[40]</sup> These discrepancies ( $\Delta E_{\text{corr}}^{\text{HL}} = \Delta H_{\text{exp}}^{\text{HL}}(T_{1/2}) - [\Delta E_{\text{el}}^{\text{HL}}(0) + \Delta E_{\text{vib}}^{\text{HL}}(T_{1/2})]$ ), possibly more important for optimized geometries, can be related to the methodology and also to the neglect in the calculations of the effect of the environment (counterions, solvent, and other neighboring molecules). Thus, a slight energy correction of  $\Delta E_{\text{corr}}^{\text{HL}} = + 500 \text{ cm}^{-1}$  applied to the calculated energies, leads to a spin transition process occurring at a transition temperature equal to that observed (for **1**,  $T_{1/2} = 92.5 \text{ K}$ ). The  $\Delta E_{\text{corr}}$  is of the order of thousands of  $\text{cm}^{-1}$ , namely, only 0.0001% of  $E_{\text{el}}$ .

Finally, at 92.5 K ( $T_{1/2}$ ), the values obtained for the vibrational ( $\Delta S_{\text{vib}}^{\text{HL}} = + 13.6 \text{ J mol}^{-1} \text{ K}^{-1}$ ) and electronic ( $\Delta S_{\text{el}}^{\text{HL}} = + 9.1 \text{ J mol}^{-1} \text{ K}^{-1}$ ) contributions to the entropy lead to a total enthalpy variation of  $\Delta H^{\text{HL}}(T_{1/2}) = + 2.1 \text{ kJ mol}^{-1}$ , where the energy correction has been considered.

**Electronic spectra:** The electronic spectra of **1** in the LS and HS states have been investigated by TDDFT calculations. As previously shown, the proximity between the energies of some occupied and unoccupied molecular orbitals centered on the metal and catechol fragments may account for the observation of charge-transfer bands in the visible or even in the near infrared region. In Figure 12 (HS state) and Figure 13 (LS state), the experimental spectra are compared with the theoretical ones obtained from experimental and optimized geometries, and a good agreement is found. As expected, the best agreement between experimental and theoretical spectra in the LS and HS states is found for the experimental geometries. Moreover, the difference between the theoretical spectra for the optimized and experimental geometries only consists in a shift of some transitions. In this way, some transitions overlap in the case of the opti-

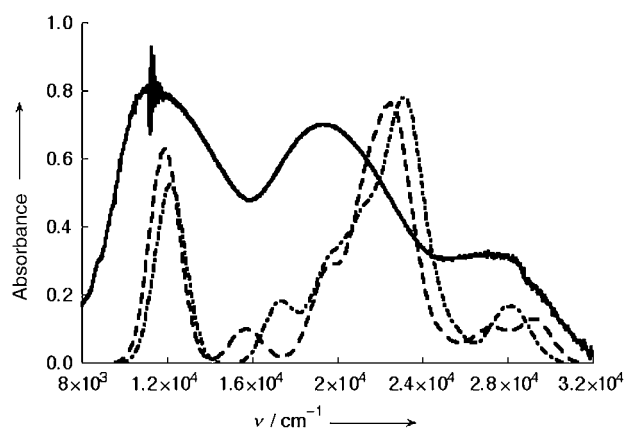


Figure 12. Corrected experimental (—) and theoretical (experimental (---) and optimized (----) geometries) spectra of the HS state.

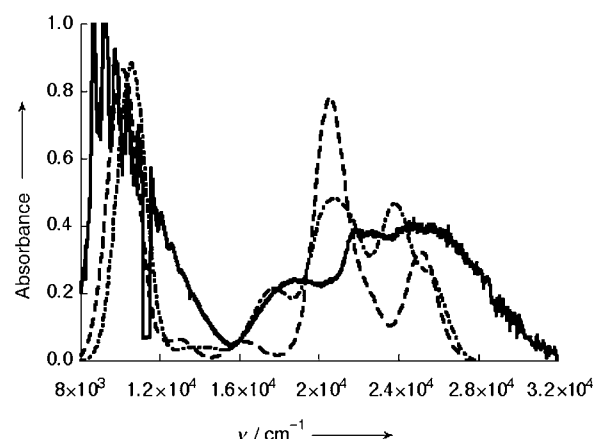


Figure 13. Corrected experimental (—) and theoretical (experimental (---) and optimized (----) geometries) spectra of the LS state.

mized geometry (LS and HS states) leading to an increase of the band intensities. These shifts are bathochromic and hypsochromic in the LS and HS states, respectively. They can be attributed to the quality of the basis sets used to construct the atomic orbitals, the chosen density functional, etc. However, it is very likely that the main factor is the exclusion of environmental effects. A detailed analysis of the more intense transitions for the HS and LS states of **1**, in the optimized and experimental geometries, is shown in Table S4 and Table S5 in the Supporting Information.

In spite of the differences between the electronic configurations of the LS and HS states, the electronic spectra present similar features with a shift of the corresponding transition energies. This is especially remarkable for the optimized geometry, for which the shapes of the theoretical spectra for the HS and LS states are very close (Figure 12 and Figure 13). The difference mainly concerns the transitions involving the d-metal orbitals (i.e. CT or dd transitions). The high-intensity transitions observed in the HS and LS states must be of the same kind, involving the same or similar molecular orbitals in both states. A narrow band is observed in the low-energy region of the experimental spectrum. The theoretical study indicates that this band mainly originates from a metal-to-ligand charge-transfer (MLCT) transition which occurs from the *beta*  $d_{xz}$  metal spin orbital to a dioxolene *beta*  $\pi$ -antibonding spin orbital (full  $117\beta$  to empty  $118\beta$  in the LS state). The theoretical bathochromic shift for this band in the LS state is probably attributable to the shorter metal-TPA bond lengths that increase the antibonding contributions in the initial  $d_{xz}$  molecular orbital and decrease the energy gap between the molecular orbitals involved in this transition. This bathochromic shift is also observed in the experimental spectra. The  $11000\text{--}16000 \text{ cm}^{-1}$  region contains the expected d-d transitions (from  $115a$  and  $116a$  to  $125a$ ,  $126a$ ,  $125\beta$ , and  $126\beta$ , Figure 11) which are masked by the tail of more intense CT bands. The intense bands observed at higher energies are assigned to  $\text{Fe}^{\text{II}} \rightarrow \text{TPA CT}$  transitions (MLCT), for which the electronic density is displaced from the  $t_{2g}$  orbitals ( $116\beta$  and  $117\beta$ ) to the

antibonding  $\pi$ -ligand orbitals ( $119\beta$ ,  $120\beta$ ,  $121\beta$  and  $122\beta$ ). These transitions also present a weak contribution of dioxolene  $\rightarrow$  TPA CT transitions ( $LL'CT$ ;  $118\alpha$  and  $117\beta$  to  $120\alpha$  and  $120\beta$ ). The latter are more numerous in the high-energy range ( $25\,000$ – $26\,000\text{ cm}^{-1}$ ), appearing as shoulders of the more intense CT band. As mentioned for the  $Fe^{II} \rightarrow SQ$  CT transitions (MLCT), the  $Fe^{II} \rightarrow TPA$  CT transitions (ML'CT) of the LS state are observed at lower energy.

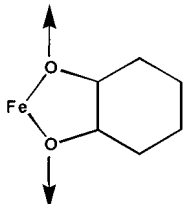
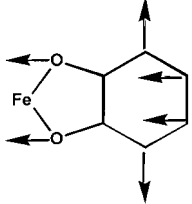
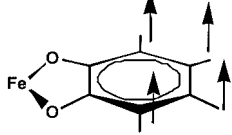
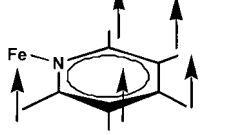
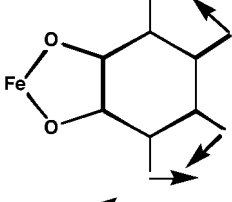
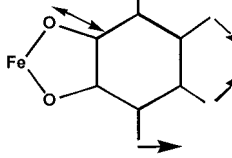
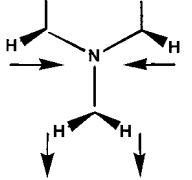
**Resonance Raman spectra and vibronic coupling:** A vibrational frequency calculation has been performed to analyze the RR spectra of **1** and to determine the vibrational modes involved in the vibronic coupling. A summary of the more intense vibrational modes in the studied region is shown in Table 6. Our calculations qualitatively agree with the results obtained by Öhrström et al. for a simpler complex.<sup>[23]</sup> In the following analysis based on the experimental data collected at 15 K, we have only considered the vibrational frequencies of the LS state, although those calculated for the HS state are also displayed in Table 6. A unique frequency at  $517\text{ cm}^{-1}$  corresponds to a vibrational mode assigned to the five-membered ring, which is a mixture of Fe–O stretching and bending modes ( $\delta$ ,  $\nu$  chelate). From this analysis, it is unambiguously identified as the vibrational mode involved in the vibronic coupling that was experimentally characterized. This mode is less energetic for the HS state than for the LS state because the Fe–O bond lengths are longer in the first case. Bands at  $585$  and  $599\text{ cm}^{-1}$  ( $\nu_{ring}$ ) are attributed to the vibrational modes arising from the deformation of the catecholate ring by means of a combination of a Fe–O and C–C stretching and ring-bending modes. The vibrational mode appearing at higher energy ( $781\text{ cm}^{-1}$ ) corresponds to the *out-of-plane* bending of the hydrogen atoms with regard to the catecholate ring ( $\delta_{CH}$ ). The equivalent vibrational mode of TPA aromatic rings is observed in the same energy region ( $\approx 798\text{ cm}^{-1}$ ). The *in-plane* hydrogen-bending modes for the catecholate and pyridine rings are displayed within the range of  $1170$ – $1270\text{ cm}^{-1}$  ( $\delta'_{CH}$ ). Fe–O stretching is coupled to some of the last vibrational modes ( $\delta'_{CH} + \nu_{CO}$ ). Some of these vibrational modes are coupled with C–C stretching modes in the rings that appear in the  $1450$ – $1600\text{ cm}^{-1}$  range. Finally, we note that the theoretical intensities are higher for the LS state than for the HS state, in agreement with the experimental observations.

## Conclusion

The spin interconversion of  $[(TPA)Fe(Cat)]BPh_4$  between the thermally accessible HS state and the LS ground state results in consequent changes of electronic, vibrational, magnetic, and structural properties in the solid state. They were characterized by means of variable-temperature UV/Vis, resonance Raman, and Mössbauer measurements in conjunction with temperature-dependent X-ray crystallography.

The electronic spectrum of the LS species presents a NIR charge-transfer band that exhibits a bathochromic shift with

Table 6. Analysis of the vibrational modes observed in the RR spectra. The experimental frequencies are compared to the values calculated for the LS and HS states.

Assignment	Exp [ $\text{cm}^{-1}$ ]	LS [ $\text{cm}^{-1}$ ]	HS [ $\text{cm}^{-1}$ ]	Scheme
$\delta$ , $\nu$ chelate	538	517	478	
$\nu$ ring	613	585–599	587–598	
$\delta$ CH (cat)	792	781	784	
$\delta$ CH (TPA)	792	798	$\sim 795$	
$\delta'$ CH (cat)	1220–1245	1170	1171	
$\delta'$ CH (cat) + $\nu$ CO	1250	1254–1262	$\sim 1260$	
$\delta$ CH <sub>2</sub>	1270	1264	1260	

respect to the HS band and possesses a well-resolved vibrational progression with individual components separated by  $520$ – $560\text{ cm}^{-1}$ . This progression also observed in the luminescence spectrum detected by the 15 K RR measurements (excitation with  $1064\text{ nm}$ ) was assigned to the five-membered chelate ring-mode  $FeO_2C_2$ .

With regard to the spin-crossover process, the analysis of the structural data reveals the presence of two nonequa-

lent crystallographic sites within the lattice. This characteristic, common to systems exhibiting a two-step spin crossover, accounts for successive transitions of the two different molecules. Such a process was shown to occur in the temperature range of the first step. Numerous intermolecular contacts and  $\pi$ -stacking interactions contribute to reinforce the cooperative interactions at low temperatures.

Some features reported in a previous communication were in favor of a Fe<sup>III</sup>-catecholate formulation of the electronic ground state of [(TPA)Fe(Cat)]BPh<sub>4</sub>. To obtain further insight into the properties of this system, DFT calculations were performed on a set of experimental structural data as well as on optimized geometries in the LS and the HS phases. Different computational results do not support the first Fe<sup>III</sup>-catecholate description, but they strongly suggest that the electronic structure consists of a mixture of Fe<sup>III</sup>-catecholate and Fe<sup>II</sup>-semiquinonate configurations. The calculations indicated abnormal spin density on the iron moiety as well as on the dioxolene ligand. The DFT analysis of the Fe<sup>II</sup>-SQ configuration also indicates a ferromagnetic coupling between the HS metal ion and the semiquinone radical leading to the relative stabilization of the  $S = 5/2$  spin state. The general features observed in UV/Vis and RR spectra were nicely reproduced by the calculations. Somewhat unexpectedly, the computational results show that the low-energy absorption band (in the HS and LS state) is not only attributable to a ligand-to-metal charge-transfer transition but to a prevailing MLCT contribution that results from the above-mentioned mixture of configurations. From the calculation of the different vibrational modes of the HS and LS species, it was confirmed that the mode responsible for the vibronic progression observed in the LS electronic spectrum is attributable to the five-membered chelate ring mode. Finally, the finding of a significant mixture of Fe<sup>III</sup>-catecholate and Fe<sup>II</sup>-semiquinonate configurations supports the general assumption commonly proposed from the analysis of the reactivity of these Fe<sup>III</sup>-catecholate dioxygenase mimics. Nevertheless, the mixture of configurations identified here from DFT calculations, and possibly accounting for subtle effects in structural and Mössbauer data, deserves to be specified further by means of, for example, combined Mössbauer in presence of magnetic field and EPR investigations together with DFT calculations on related compounds with catecholate groups with different donor or acceptor substituents.

## Experimental Section

**Synthesis:** The TPA ligand and the [(TPA)Fe(Cat)]BPh<sub>4</sub> complex (**1**) were prepared following already described procedures.<sup>[6,43]</sup>

**UV/Vis spectrometry:** UV/Vis absorption measurements of KBr pellets were recorded with a Varian CARY 5E double-beam spectrophotometer, equipped with an APD Cryogenics closed-cycle helium cryogenic system including a DMX-1E cryostat and a DE-202 expander instrument. The KBr pellets were prepared with 3% of **1** dispersed into the KBr powder. Grinding of the solid was avoided as it may have resulted in the chemical and/or physical alteration of the sample.

**Resonance Raman spectroscopy:** Resonance Raman spectra were recorded on two different spectrometers, depending on the excitation wavelength used. Spectra excited with the 1064 nm line of a diode-pumped Nd:YAG laser were recorded on a Bruker IFS66 interferometric Fourier-transform Raman spectrometer equipped with a FRA106 Raman module with a liquid nitrogen-cooled Ge diode detector as described elsewhere.<sup>[44]</sup> Typically, 180 mW of laser power was used at the sample, which was contained in a cryostat in which cold He gas was circulating (TBT, France) and was held at various temperatures ranging from 15 K to room temperature. The sample was in the form of a slightly compressed powder held in a sample holder. No evidence of spectral modification that would indicate sample degradation was observed during up to two hours of observation under laser irradiation. Spectra were recorded with 752.5 nm excitation by means of a Kr<sup>+</sup> laser (Coherent Innova90) and a modified Jobin-Yvon T64000 dispersive Raman spectrometer equipped with a back-illuminated liquid nitrogen-cooled CCD detector, and only one stage with 900 lines mm<sup>-1</sup> grating. Typically, 50 mW of laser power was used at the sample held in a similar cryostat (STVP-100, Janis Research); the temperature was varied between 15 K and 270 K.

**X-ray diffraction:** A crystal with an approximate size of 0.150 × 0.100 × 0.050 mm was selected. The crystal structure was solved at temperatures of 220(2) and 110(2) K, for which the fractions of HS species estimated from the magnetic data (with  $\chi T_{LS} = 0.375 \text{ cm}^3 \text{ mol}^{-1} \text{ K}$  and  $\chi T_{HS} = 4.375 \text{ cm}^3 \text{ mol}^{-1} \text{ K}$ ) are  $\gamma_{HS} = 0.92$  (220 K) and 0.66 (110 K). Diffraction data were collected with a Nonius diffractometer equipped with a CCD detector. The lattice parameters were determined from ten images recorded with  $2^\circ \Phi$  scans and later refined on all data. A  $180^\circ \Phi$  range was scanned, with  $2^\circ$  steps, with the crystal-to-detector distance fixed at 30 mm. Data were corrected for Lorentz polarization. The structure was solved by direct methods and refined by full-matrix least-squares on  $F^2$  with anisotropic thermal parameters for iron atoms. H atoms were introduced at calculated positions and constrained to ride on their parent C atoms. All calculations were performed on an O2 Silicon graphics station with the SHELXTL package.<sup>[45]</sup>

Formula: C<sub>48</sub>H<sub>42</sub>BF<sub>4</sub>FeN<sub>4</sub>O<sub>2</sub>;  $MW = 773.52$ ,  $\lambda(\text{Mo}_{K\alpha}) = 0.71073 \text{ \AA}$ ; crystallographic system: orthorhombic and space group:  $Pca2(1)$  for both temperatures.

For  $T = 220(2) \text{ K}$ :  $a = 29.427(6)$ ,  $b = 9.449(2)$ ,  $c = 28.093(6)$ ,  $V = 7811(3) \text{ \AA}^3$ ,  $Z = 8$ ,  $\rho = 1.315 \text{ g cm}^{-3}$ ,  $\mu = 0.432 \text{ mm}^{-1}$ ,  $\theta_{\text{max}} = 22.69^\circ$ ; index ranges:  $0 \leq h \leq 31$ ,  $0 \leq k \leq 9$ ,  $0 \leq l \leq 30$ ; 35950 measured reflections, 5190 independent reflections, 2942 reflections observed with  $I > 2\sigma(I)$ , 459 parameters,  $R1 = 0.086$ ;  $wR2 = 0.186$ .

For  $T = 110(2) \text{ K}$ :  $a = 29.324(6)$ ,  $b = 9.400(2)$ ,  $c = 27.840(6)$ ,  $V = 7674(3) \text{ \AA}^3$ ,  $Z = 8$ ,  $\rho = 1.339 \text{ g cm}^{-3}$ ,  $\mu = 0.440 \text{ mm}^{-1}$ ,  $\theta_{\text{max}} = 22.73^\circ$ ; index ranges:  $0 \leq h \leq 31$ ,  $0 \leq k \leq 9$ ,  $0 \leq l \leq 30$ , 36394 measured reflections, 5083 independent reflections, 3205 reflections observed with  $I > 2\sigma(I)$ , 459 parameters,  $R1 = 0.085$ ,  $wR2 = 0.178$  ( $R1 = \sum ||F_o| - |F_c|| / \sum |F_o|$ ); ( $wR2 = \{\sum [w(F_o^2 - F_c^2)]^2 / \sum [wF_o^2]\}^{1/2}$  with  $w = 1/[\sigma^2(F_o^2) + (0.0744P)^2 + 1.1323P]$ , whereby  $P = (F_o^2 + 2F_c^2)/3$ ).

CCDC-238902 and CCDC-238903 contain the supplementary crystallographic data for this paper. These data can be obtained free of charge via [www.ccdc.cam.ac.uk/conts/retrieving.html](http://www.ccdc.cam.ac.uk/conts/retrieving.html) (or from the Cambridge Crystallographic Data Centre, 12 Union Road, Cambridge CB21EZ, UK; fax: (+44) 1223-336033; or deposit@ccdc.cam.ac.uk).

**Mössbauer measurements:** A constant acceleration-type Mössbauer spectrometer equipped with a 1024-channel analyzer operating in the time-scale mode, and a 25 mCi <sup>57</sup>Co/Rh source were employed. The isomer shifts reported here are relative to  $\alpha\text{Fe}$  at room temperature. Spectra of the samples (thickness of  $\approx 5 \text{ mg Fe cm}^{-2}$ ) were collected between 293 and 1.9 K by means of a combined He continuous flow/bath cryostat. The Mössbauer spectra were analyzed with the RECOIL computer program.<sup>[46]</sup>

**Density functional calculations:** All theoretical calculations were carried out with the hybrid B3LYP method,<sup>[47]</sup> as implemented in the GAUSSIAN98 program.<sup>[48]</sup> Double- $\zeta$  and triple- $\zeta$  quality basis sets proposed by Ahlrichs and co-workers have been employed for non-metal and metal atoms, respectively.<sup>[49]</sup> Also, two extra polarization  $p$  functions have been added for the metal atom. The calculations were performed on the

[(TPA)Fe(Cat)]<sup>+</sup> complex (**1**) in the LS and HS states. The geometries of **1** in the two spin states have been fully optimized. Moreover, single-point calculations on the experimental geometries have also been performed. Thus, the experimental geometries of the B site in the crystal structure at 220 and 110 K have been considered in the calculations for the HS and LS states, respectively. The atomic spin densities were obtained from a natural bond orbital (NBO) analysis.<sup>[50]</sup> The theoretical electronic spectra have been simulated from the energy of the excited states and oscillator strengths calculated by the time-dependent DFT formalism as implemented in the GAUSSIAN98 program.<sup>[48,51]</sup> A value equal to 2000 cm<sup>-1</sup> for the bandwidth at half-height has been used in these simulations because this value often provides molar extinction coefficient values of the same order of magnitude as the experimental ones. The experimental spectra have been corrected in order to compare them with the theoretical ones: the background absorbance usually present in electronic spectra in the solid phase has been removed, as well as the bands located out of the selected energy range (8000–33 000 cm<sup>-1</sup>). The vibrational frequencies have been computed in the LS and HS states from the optimized geometries in order to analyze the Raman spectra and the vibronic coupling observed in the electronic spectra.

### Acknowledgements

The authors thank Dr. M. Nierlich for the single-crystal X-ray measurements. Prof. H. Güdel and A. Hauser are gratefully acknowledged for very fruitful discussions and Dr. F. Banse and R. Guillot are acknowledged for their helpful comments on the manuscript. T.A.M. is grateful to the Regional Council of the Ile-de-France for an equipment grant (S.E.S.A.M.E.). Some of us are also grateful to the European Science Foundation, the European TMR program (ERB-FMRX-CT98-0199).

- [1] J. D. Lipscomb, A. M. Orville in *Metal Ions in Biological Systems*, Vol. 28, (Eds.: A. Sigel, H. Sigel), Marcel Dekker, New York, Basel, **1992**, p. 243.
- [2] L. Que, Jr. in *Bioinorganic Catalysis*, 2nd ed.; (Eds.: J. Reedijk, E. Bouwman), Marcel Dekker, New York, **1999**, p. 269; L. Que, Jr., M. F. Reynolds in *Metal Ions in Biological Systems*, Vol. 37, (Eds.: A. Sigel, H. Sigel), Marcel Dekker, New York, Basel, **2000**, p. 505.
- [3] H. J. Krüger in *Biomimetic Oxidations Catalyzed by Transition Metal Complexes* (Ed.: B. Meunier), Imperial College Press, London, **2000**, 363; “*Oxygenases and Model Systems*”, T. Funabiki in *Catalysis by Metal complexes*, Vol. 19, (Eds.: R. Ugo, B. R. James), Kluwer Academic Publishers, Dordrecht, **1997**, pp. 1–393.
- [4] E. I. Solomon, T. C. Brunold, M. I. Davis, J. N. Kemsley, S. K. Lee, N. Lehnert, F. Neese, A. J. Skulan, Y. S. Yang, J. Zhou, *Chem. Rev.* **2000**, *100*, 235.
- [5] a) D. D. Cox, L. Que, Jr., *J. Am. Chem. Soc.* **1988**, *110*, 8085; b) D. D. Cox, S. J. Benkovic, L. M. Bloom, F. C. Bradley, M. J. Nelson, L. Que, Jr., D. E. Wallick, *J. Am. Chem. Soc.* **1988**, *110*, 2026; c) H. G. Jang, D. D. Cox, L. Que, Jr., *J. Am. Chem. Soc.* **1991**, *113*, 9200; d) L. Que, Jr., R. Y. N. Ho, *Chem. Rev.* **1996**, *96*, 2607.
- [6] A. J. Simaan, M.-L. Boillot, E. Rivière, A. Boussac, J.-J. Girerd, *Angew. Chem.* **2000**, *112*, 202; *Angew. Chem. Int. Ed.* **2000**, *39*, 196.
- [7] a) T. Funabiki, A. Mizoguchi, T. Sugimoto, S. Tada, M. Tsuji, H. Sakamoto, S. Yoshida, *J. Am. Chem. Soc.* **1986**, *108*, 2921; b) T. Funabiki, A. Fukui, Y. Hitomi, M. Higuchi, T. Yamamoto, T. Tanaka, F. Tani, Y. Naruta, *J. Inorg. Biochem.* **2002**, *91*, 151.
- [8] a) T. M. H. Bugg, G. Lin, *Chem. Commun.* **2001**, 941; b) C. J. Winfield, Z. Al-Mahrizy, M. Gravestock, T. D. H. Bugg, *J. Chem. Soc. Perkin Trans. 1* **2000**, 3277.
- [9] a) P. Gütllich, H. Spiering, A. Hauser in *Inorganic Electronic Structure and Spectroscopy*, Vol. II (Eds.: E. I. Solomon, A. B. P. Lever), VCH, Weinheim, **1999**, p. 575; b) *Molecular Magnetism*, (Ed.: O. Kahn), VCH, New York, **1993**, p. 53; c) M. Bacci, *Coord. Chem. Rev.* **1988**, *86*, 245; d) J. K. Beattie, *Adv. Inorg. Chem.* **1988**, *32*, 1;
- e) H. Toftlund, *Coord. Chem. Rev.* **1989**, *94*, 67; f) J. Zarembowitch, *New J. Chem.* **1992**, *16*, 255.
- [10] a) M. S. Haddad, W. D. Federer, M. W. Lynch, D. N. Hendrickson, *Inorg. Chem.* **1981**, *20*, 123; b) M. D. Timken, S. R. Wilson, D. N. Hendrickson, *Inorg. Chem.* **1985**, *24*, 3450.
- [11] a) E. König, G. Ritter, S. K. Kulshreshtha, *Chem. Rev.* **1985**, *85*, 219; b) E. König, *Prog. Inorg. Chem.* **1987**, *35*, 527.
- [12] The two-step spin crossover, often observed in conjunction with a phase transition, was characterized for a number of compounds having nonequivalent crystallographic sites in the asymmetric unit. Each of these sites identified in a temperature range or at all temperatures play a specific role in the HS⇌LS transition. These features also account for the properties of the very first example of a two-step spin-crossover compound [Fe<sup>II</sup>(2-pic)<sub>3</sub>]Cl<sub>2</sub>·EtOH (pic = 2-picolyamine). For a long time, this compound was considered to be a unique case because only one iron site and the same space group were detected in the high- and low-temperature phases. The very detailed and accurate structural determination recently reported by Bürgi and co-workers provides new insight into the factors that cause the two-step process. Indeed the spin-crossover transformation was shown to be coupled to two successive order–disorder transitions that leads, in the ordered intermediate phase, to two different iron sites characterized by different spin states.
- [13] a) D. Boinnard, A. Bousseksou, A. Dworkin, J.-M. Savariault, F. Varret, J.-P. Tuchagues, *Inorg. Chem.* **1994**, *33*, 271; b) Y. Garcia, O. Kahn, L. Rabardel, B. Chansou, L. Salmon, J.-P. Tuchagues, *Inorg. Chem.* **1999**, *38*, 4663; c) M. Yamada, M. Ooidemizu, Y. Ikuta, S. Osa, N. Matsumoto, S. Iijima, M. Kojima, F. Dahan, J.-P. Tuchagues, *Inorg. Chem.* **2003**, *42*, 8406.
- [14] a) H. Köppen, E. W. Müller, C. P. Köhler, H. Spiering, E. Meissner, P. Gütllich, *Chem. Phys. Lett.* **1982**, *91*, 348; b) D. Chernyshov, M. Hostettler, K. W. Törnroos, H.-B. Bürgi, *Angew. Chem.* **2003**, *115*, 3955; *Angew. Chem. Int. Ed.* **2003**, *42*, 3825.
- [15] a) C. G. Pierpont, *Coord. Chem. Rev.* **2001**, *216–217*, 99; b) C. G. Pierpont, *Coord. Chem. Rev.* **2001**, *219–221*, 415.
- [16] a) D. M. Adams, A. Dei, A. L. Rheingold, D. N. Hendrickson, *J. Am. Chem. Soc.* **1993**, *115*, 8221; b) D. M. Adams, D. N. Hendrickson, *J. Am. Chem. Soc.* **1996**, *118*, 11515; c) D. M. Adams, L. Noodleman, D. N. Hendrickson, *Inorg. Chem.* **1997**, *36*, 3966.
- [17] The spectrum of this compound was also recorded in a Vaseline mull to address the question of a possible alteration of the solid sample dispersed in KBr. The absence of a significant change between the RT (see Figure S1 in the Supporting Information) and also the low-temperature spectra indicates that the solid dispersion into KBr gives rise to minor effects on the molecular properties.
- [18] A. Dei, D. Gatteschi, L. Pardi, *Inorg. Chem.* **1993**, *32*, 1389.
- [19] a) S. Schenker, A. Hauser, *J. Am. Chem. Soc.* **1994**, *116*, 5497; b) S. Schenker, A. Hauser, R. M. Dyson, *Inorg. Chem.* **1996**, *35*, 4676.
- [20] T. C. Brunold, H. U. Güdel in *Inorganic Electronic Structure and Spectroscopy*, Vol. I (Eds.: E. I. Solomon, A. B. P. Lever), VCH, Weinheim, **1999**, p. 259.
- [21] a) I. Michaud-Soret, K. K. Andersson, L. Que Jr., J. Haavik, *Biochemistry* **1995**, *34*, 5504; b) S. Salama, J. D. Stong, J. B. Neilands, T. G. Spiro, *J. Am. Chem. Soc.* **1978**, *100*, 3781; c) J. W. Pyrz, A. L. Roe, L. J. Stern, L. Que Jr., *J. Am. Chem. Soc.* **1985**, *107*, 614; d) B. P. Gaber, V. Miskowski, T. G. Spiro, *J. Am. Chem. Soc.* **1974**, *96*, 6868.
- [22] K. Nakamoto, *Infrared Spectra of Inorganic and Coordination Compounds*, Wiley-Interscience, New York, **1986**.
- [23] a) L. Öhrström, I. Michaud-Soret, *J. Am. Chem. Soc.* **1996**, *118*, 3283; b) L. Öhrström, I. Michaud-Soret, *J. Phys. Chem. A* **1999**, *103*, 256.
- [24] a) A. Hauser in *Spin-Crossover in Transition Metal Compounds*, Topics in Current Chemistry, Springer, (Eds.: P. Gütllich, H. Goodwin), **2004**; b) S. Decurtins, P. Gütllich, K. M. Hasselbach, H. Spiering, A. Hauser, *Inorg. Chem.* **1985**, *24*, 2174; c) A. Hauser, J. Jeftic, H. Romstedt, R. Hinek, H. Spiering, *Coord. Chem. Rev.* **1999**, *190–192*, 471.

- [25] S. Hayami, Z.-Z. Gu, M. Shiro, Y. Einaga, A. Fujishima, O. Sato, *J. Am. Chem. Soc.* **2000**, *122*, 7126.
- [26] a) L. Que, Jr., R. C. Kolanczyk, L. S. White, *J. Am. Chem. Soc.* **1987**, *109*, 5373; b) W. O. Koch, H. J. Krüger, *Angew. Chem.* **1995**, *107*, 2928; *Angew. Chem. Int. Ed. Engl.* **1995**, *34*, 2671; c) P. Mialane, L. Tchertanov, F. Banse, J. Sainton, J.-J. Girerd, *Inorg. Chem.* **2000**, *39*, 2440; d) D. H. Jo, Y.-M. Chiou, L. Que, Jr., *Inorg. Chem.* **2001**, *40*, 3181; e) M. Pascaly, M. Duda, F. Schweppe, K. Zurlinden, F. K. Müller, B. Krebs, *J. Chem. Soc. Dalton Trans.* **2001**, 828; f) M. Merkel, F. K. Müller, B. Krebs, *Inorg. Chim. Acta* **2002**, *337*, 308.
- [27] The structural parameters found in the literature for HS Fe<sup>III</sup>Cat (or Fe<sup>II</sup>SQ) systems are C–O 1.295–1.355 (1.275–1.290), C–C 1.389–1.399 (1.402–1.440), and C21–C22 1.369–1.400 Å (1.383–1.446).
- [28] a) R. M. Buchanan, S. L. Kessel, H. H. Downs, C. G. Pierpont, D. N. Hendrickson, *J. Am. Chem. Soc.* **1978**, *100*, 7894; b) S. R. Boone, G. H. Purser, H. R. Chang, M. D. Lowery, D. N. Hendrickson, C. G. Pierpont, *J. Am. Chem. Soc.* **1989**, *111*, 2292; c) A. S. Attia, B. J. Conklin, C. W. Lange, C. G. Pierpont, *Inorg. Chem.* **1996**, *35*, 1033; d) W. O. Koch, V. Schünemann, M. Gerdan, A. X. Trautwein, H. J. Krüger, *Chem. Eur. J.* **1998**, *4*, 1255.
- [29] a) Y. Nishida, K. Kino, S. Kida, *J. Chem. Soc. Dalton Trans. J. Chem. Soc. Dalton Trans.* **1987**, 1957; b) H. Oshio, K. Toriumi, Y. Maeda, Y. Takashima, *Inorg. Chem.* **1991**, *30*, 4252; c) A. J. Conti, R. K. Chadha, K. M. Sena, A. L. Rheinhold, D. N. Hendrickson, *Inorg. Chem.* **1993**, *32*, 2670.
- [30] a) P. Poganiuch, S. Decurtins, P. Gütllich, *J. Am. Chem. Soc.* **1990**, *112*, 3270; b) R. Hinek, H. Spiering, D. Schollmeyer, A. Hauser, *Chem. Eur. J.* **1996**, *2*, 1427.
- [31] a) J.-F. Létard, P. Guionneau, E. Codjovi, O. Lavastre, G. Bravic, D. Chasseau, O. Kahn, *J. Am. Chem. Soc.* **1997**, *119*, 10861; b) Z. J. Zhong, J.-Q. Tao, Z. Yu, C.-Y. Dun, Y.-J. Liu, X.-Z. You, *J. Chem. Soc. Dalton Trans.* **1998**, 327.
- [32] E. Münck in *Physical Methods in Bioinorganic Chemistry* (Ed.: L. Que, Jr.), University Science Books, Sausalito, **2000**, p. 287.
- [33] a) M. Pascaly, M. Duda, A. Rompel, B. H. Sift, W. Meyer-Klaucke, B. Krebs, *Inorg. Chim. Acta* **1999**, *291*, 289; b) E. W. Ainscough, A. M. Brodie, J. E. Plowman, K. L. Brown, A. W. Addison, A. R. Gainsford, *Inorg. Chem.* **1980**, *19*, 3655; c) A. K. Boudalis, F. Dahan, A. Bousseksou, J.-P. Tuchagues, S. P. Perlepes, *Dalton Trans.* **2003**, 3411.
- [34] a) M. J. Cohn, C.-L. Xie, J.-P. Tuchagues, C. G. Pierpont, D. N. Hendrickson, *Inorg. Chem.* **1992**, *31*, 5028; b) P. Mialane, E. Anxolabéhère-Mallart, G. Blondin, A. Nivorojkine, J. Guilhem, L. Tchertanova, M. Cesario, N. Ravi, E. Bominaar, J.-J. Girerd, E. Münck, *Inorg. Chim. Acta* **1997**, *263*, 367.
- [35] [(TPA)Fe(Cl<sub>4</sub>Cat)]PF<sub>6</sub> (**2**) crystallizes in an orthorhombic space group *Pna2(1)/c* (*Z* = 4), which is retained at 123 K. As shown by the selected metal–ligand bond lengths in Table S3 in the Supporting Information, the FeN<sub>4</sub>O<sub>2</sub> core adopts a distorted octahedral geometry. This compound exhibits a smooth spin-crossover process which spreads over a temperature range greater than 200 K. The transition temperature ( $\gamma_{\text{HS}} = \gamma_{\text{LS}} = 0.5$ ) is 204 K. The values of  $\chi_{\text{M}}T$  are equal to 0.698 cm<sup>3</sup> mol<sup>-1</sup> K and 3.661 cm<sup>3</sup> mol<sup>-1</sup> K at 5 and 300 K respectively.
- [36] S. Floquet, Ph. D. Thesis, Université Paris-Sud, Orsay, (France) **2001**.
- [37] P. Ghosh, A. Begum, D. Herebian, E. Bothe, K. Hildenbrand, T. Weyhermüller, K. Wieghardt, *Angew. Chem.* **2003**, *115*, 581; *Angew. Chem. Int. Ed.* **2003**, *42*, 563.
- [38] J. H. Rodriguez, D. E. Wheeler, J. K. McCusker, *J. Am. Chem. Soc.* **1998**, *120*, 12051.
- [39] K. Chen, M. Costas, L. Que, Jr., *J. Chem. Soc. Dalton Trans.* **2002**, 672.
- [40] a) H. Paulsen, H. Grünsteudel, W. Meyer-Klaucke, M. Gerdan, H. F. Grünsteudel, A. I. Chumakov, R. Rüffer, H. Winkler, H. Toftlund, A. X. Trautwein, *Eur. Phys. J. B* **2001**, *23*, 463; b) H. Paulsen, R. Benda, C. Herta, V. Schünemann, A. I. Chumakov, L. Duelund, H. Winkler, H. Toftlund, A. X. Trautwein, *Phys. Rev. Lett.* **2001**, *86*, 1351. H. Paulsen, A. X. Trautwein, *J. Phys. Chem. Solids* **2004**, *65*, 793.
- [41] A. I. Chumakov, R. Rüffer, O. Leupold, H. Grünsteudel, A. Barla, T. Asthalter, ESRF Highlights-1999, ESRF, Grenoble, (France) **2000**.
- [42] R. Carrasco, I. Morgenstern-Badarau, J. Cano, *Chem. Commun.* **2003**, 436.
- [43] B. G. Gafford, R. A. Holwerda, *Inorg. Chem.* **1989**, *28*, 60.
- [44] T. A. Mattioli, X. Lin, J. P. Allen, J. C. Williams, *Biochemistry* **1995**, *34*, 6142.
- [45] G. M. Sheldrick, SHELXTL-97, program for the refinement of crystal structures, University of Göttingen (Germany), **1997**.
- [46] K. Lagarec, D. G. Rancourt, Department of Physics, University of Ottawa, **1998**.
- [47] A. D. Becke, *J. Chem. Phys.* **1993**, *98*, 5648.
- [48] Gaussian 98, Revision A.7: M. J. Frisch, G. W. Trucks, H. B. Schlegel, G. E. Scuseria, M. A. Robb, J. R. Cheeseman, V. G. Zakrzewski, J. A. Montgomery, Jr., R. E. Stratmann, J. C. Burant, S. Dapprich, J. M. Millam, A. D. Daniels, K. N. Kudin, M. C. Strain, O. Farkas, J. Tomasi, V. Barone, M. Cossi, R. Cammi, B. Mennucci, C. Pomelli, C. Adamo, S. Clifford, J. Ochterski, G. A. Petersson, P. Y. Ayala, Q. Cui, K. Morokuma, D. K. Malick, A. D. Rabuck, K. Raghavachari, J. B. Foresman, J. Cioslowski, J. V. Ortiz, A. G. Baboul, B. B. Stefanov, G. Liu, A. Liashenko, P. Piskorz, I. Komaromi, R. Gomperts, R. L. Martin, D. J. Fox, T. Keith, M. A. Al-Laham, C. Y. Peng, A. Nanayakkara, C. Gonzalez, M. Challacombe, P. M. W. Gill, B. Johnson, W. Chen, M. W. Wong, J. L. Andres, C. Gonzalez, M. Head-Gordon, E. S. Replogle, J. A. Pople, Gaussian, Inc., Pittsburgh, PA, **1998**.
- [49] a) A. Schaefer, H. Horn, R. Ahlrichs, *J. Chem. Phys.* **1992**, *97*, 2571; b) A. Schaefer, H. Huber, R. Ahlrichs, *J. Chem. Phys.* **1994**, *100*, 5829.
- [50] a) J. E. Carpenter, F. Weinhold, *J. Mol. Struct.* **1988**, *169*, 41; b) A. E. Reed, L. A. Curtis, F. Weinhold, *Chem. Rev.* **1988**, *88*, 899; c) F. Weinhold, J. E. Carpenter in *Structure of Small Molecules and Ions* (Eds.: R. Naaman, Z. Vager), Plenum, **1988**, p. 227.
- [51] M. E. Casida, C. Jamorski, K. C. Casida, D. R. Salahub, *J. Chem. Phys.* **1998**, *108*, 4439.

Received: May 17, 2004

Revised: October 19, 2004

Published online: January 25, 2005